

MY SHITTY THESIS WITH MANY COMPLICATED AND INCONCLUSIVE PROJECTS THAT WILL END UP HAVING A LONG TITLE

TOMMASO BOSCHI

31st March 2020

Submitted in partial fulfilment of the requirements of the Degree of Doctor of Philosophy

QUEEN MARY UNIVERSITY OF LONDON

Particle Physics Research Centre, School of Physics and Astronomy

and

UNIVERSITY OF DURHAM

Institute for Particle Physics Phenomneology

I, Tommaso Boschi, confirm that the research included within this thesis is my own work or that where it has been carried out in collaboration with, or supported by others, that this is duly acknowledged below and my contribution indicated. Previously published material is also acknowledged below.

I attest that I have exercised reasonable care to ensure that the work is original, and does not to the best of my knowledge break any UK law, infringe any third party's copyright or other Intellectual Property Right, or contain any confidential material.

I accept that the College has the right to use plagiarism detection software to check the electronic version of the thesis.

I confirm that this thesis has not been previously submitted for the award of a degree by this or any other university.

The copyright of this thesis rests with the author and no quotation from it or information derived from it may be published without the prior written consent of the author.

Signature:

Date:

Details of collaboration and publications:

Abstract

This is my thesis, get over with it.

Contents

1 Neutrino in the Standard Model	6
1.1 Neutrino interactions	7
2 Experimental techniques for neutrino detections	11
2.1 Water cherenkov	11
2.2 Gadolinium neutron capture	13
2.3 Neutrino Production	15
2.4 Liquid argon time projection chamber	17
3 Continuous gadolinium measurement	18
3.1 Gadolinium sulfate	19
3.2 Gadolinium concentration	20
4 Neutron calibration with a californium source	22
5 Hyper-Kamiokande sensitivity to δ_{CP}	26
5.1 CP violation in neutrino oscillations	26
5.2 Hyper-Kamiokande experiment	27
5.3 Sensitivity to δ_{CP}	28
5.4 Systematic studies and conclusions	29
6 HNL searches at DUNE	31
6.1 Introduction	31
6.2 Heavy neutrinos in seesaw models	34
6.3 Heavy neutrino decay	36
6.3.1 Polarised Majorana neutrino decay	38
6.3.2 Polarised (pseudo-)Dirac neutrino decay	42
6.4 Heavy neutrino production	44
6.4.1 Two-body decays	45
6.4.2 Three-body decays	47

6.5	Simulation of events at DUNE ND	47
6.5.1	Flux prediction	50
6.5.2	Background evaluation	51
6.5.3	HNL decay events and signal efficiency	54
6.6	Sensitivities of DUNE ND	55
6.6.1	Single dominant mixing	56
6.6.2	Two dominant mixings	57
6.7	Mass model constraints from DUNE ND	58
6.7.1	Mass model scan	59
6.7.2	Overall sensitivity	61
6.8	List of integrals and identities	62
6.8.1	Decay widths	62
6.8.2	Scaling factors for three body-decays	63
6.9	Polarised $N \rightarrow \nu \ell_\alpha^- \ell_\beta^+$ distributions	65
6.9.1	Dirac ν_i	65
6.9.2	Dirac $\bar{\nu}_i$	65
6.9.3	Majorana N_i	65
6.10	Open charm production	66
6.11	Background reduction	67
6.11.1	Two-body decays	68
6.11.2	Three-body decays	68
6.11.3	EM-detected decays	69
A	Appendix 1	71
B	Appendix 2	72
C	Appendix 3	73

Chapter 1

Neutrino in the Standard Model

The Standard Model (SM) is a gauge theory that describes the strong, electromagnetic, and weak interactions of elementary particles in the framework of quantum field theory. The theory is based on the local symmetry group

$$\mathrm{SU}(3)_C \otimes \mathrm{SU}(2)_L \otimes \mathrm{U}(1)_Y \quad (1.1)$$

where C , L and Y denote color, left-handed chirality and weak hypercharge, respectively. The gauge group uniquely determines the interactions and the number of vector gauge bosons that correspond to the generators of the group. They are eight massless gluons that mediate strong interactions, corresponding to the eight generators of $\mathrm{SU}(3)_C$, and four gauge bosons, of which three are massive (W^\pm and Z) and one is massless, corresponding to the three generators of $\mathrm{SU}(2)_L$ and one generator of $\mathrm{U}(1)_Y$, responsible for electroweak interactions. The symmetry group of the SM fixes the interactions, i.e. the number and properties of the vector gauge bosons, with only three independent unknown parameters: the three coupling constants of the $\mathrm{SU}(3)_C$, $\mathrm{SU}(2)_L$, and $\mathrm{U}(1)_Y$ groups, all of which must be determined from experiments. On the contrary, the number and properties of scalar bosons and fermions are left unconstrained, except for the fact that they must transform according to the representations of the symmetry group, while the fermion representations must lead to the cancellation of quantum anomalies. The known elementary fermions are divided in two categories, quarks and leptons, according to the scheme:

	Generation	1st	2nd	3rd
Quark	u	c	t	
	d	s	b	
Leptons	e	μ	τ	
	ν_e	ν_μ	ν_τ	

and their respective antiparticles. They are distinguished by the fact that quarks participate in all the interactions whereas leptons participate only in the electroweak interactions.

In the SM, electroweak interactions can be studied separately from strong interactions, because

the symmetry under the color group is unbroken and there is no mixing between the $SU(3)_C$ and the $SU(2)_L \otimes U(1)_Y$ sectors. On the other hand, the Glashow, Salam, and Weinberg theory well explains the group mixing between electromagnetic and weak interactions caused by a symmetry breaking process. This model and the discovery of the predicted W and Z bosons, in addition to the gluon, the top, and charm quarks, made the fortune of the Standard Model. Their predicted properties were experimentally confirmed with good precision and the recent discovery of the Higgs Boson is the last crowning achievement of SM.

Despite being the most successful theory of particle physics to date, the SM is actually limited in its approximation to reality, in that some clear evidences cannot be explained. The most outstanding breakthrough is the neutrino oscillations, which was awarded the Nobel Prize in Physics in 2015 and has proved that the neutrinos are not all massless, as it is assumed by theory. Mass terms for the neutrinos can be included in the SM, with the implications of theoretical problems. Likewise, the SM is unable to provide an explanation of the observed asymmetry between matter and anti-matter. It was noted by Sakharov that a solution to this puzzle would require some form of C and CP violation in the early Universe, along with Baryon number violation and out-of-equilibrium interactions. These facts suggest that the Standard Model is not a complete theory and additional physics Beyond the Standard Model (BSM) is required.

The study of neutrinos is for sure one of the most promising probe to BSM physics and is of vital importance to the future development of particle physics, in particular through precision measurement of their interactions. A deep understanding of neutrino interactions, and neutrino-nucleon interactions in particular, could lead to a great impact on long-baseline experiments, proton decay search, and supernova detection.

1.1 Neutrino interactions

Neutrinos are colourless and chargless particles, thus sensitive only to weak interactions. Because of their nature, these leptons have small cross-sections and are difficult to measure. All the interactions are described by the electroweak part of the SM, based on the symmetry group $SU(2)_L \otimes U(1)_Y$, and are governed by the lagrangian $\mathcal{L} = \mathcal{L}^{(CC)} + \mathcal{L}^{(NC)}$. In fact, neutrinos are mediated by the W^\pm for charged-current (CC) interactions and by the Z boson for neutral-current (NC) ones, whose respective lagrangians are:

$$\mathcal{L}^{(CC)} = -\frac{g}{2\sqrt{2}}(j_{W,L}^\mu W_\mu + \text{h.c}) \quad (1.2)$$

$$\mathcal{L}^{(NC)} = -\frac{g}{2\cos\vartheta_W} j_{Z,\nu}^\mu Z_\mu, \quad (1.3)$$

where the two currents are given by

$$j_{W,L}^\mu = 2 \sum_{\alpha=e,\mu,\tau} \overline{\nu_{\alpha L}} \gamma^\mu l_{\alpha L} \quad (1.4)$$

$$j_{Z,\nu}^\mu = \sum_{\alpha=e,\mu,\tau} \overline{\nu_{\alpha L}} \gamma^\mu \nu_{\alpha L}, \quad (1.5)$$

and $\vartheta_W = 28.7^\circ$ is the Weinberg angle.

The easiest interaction that can be studied is the neutrino-electron elastic scattering

$$\nu_\alpha + e^- \rightarrow \nu_\alpha + e^-, \quad (1.6)$$

and its antineutrino counterpart¹. For the electronic neutrino, both CC and NC interactions are allowed, while for $\alpha = \mu, \tau$ the charged-current interactions are forbidden. The respective Feynman diagrams are shown in Fig. ?? and ???. For low neutrino energies, where the effects of the W and Z propagators can be neglected, the above processes are described by the effective charged-current and neutral-current lagrangians

$$\mathcal{L}_{\text{eff}}(\nu_e e^- \rightarrow \nu_e e^-) = -\frac{G_F}{\sqrt{2}} [\overline{\nu_e} \gamma^\mu (1 - \gamma^5) \nu_e] [\bar{e} \gamma_\mu ((1 + g_V^l) - (1 + g_A^l) \gamma^5) e] \quad (1.7)$$

$$\mathcal{L}_{\text{eff}}(\nu_\alpha e^- \rightarrow \nu_\alpha e^-) = -\frac{G_F}{\sqrt{2}} [\overline{\nu_\alpha} \gamma^\mu (1 - \gamma^5) \nu_\alpha] [\bar{e} \gamma_\mu (g_V^l - g_A^l) \gamma^5 e] \quad (\alpha = \mu, \tau). \quad (1.8)$$

The differential cross-section with respect to the momentum transfer Q^2

$$\frac{d\sigma}{dQ^2} = \frac{G_F^2}{\pi} \left[g_1^2 + g_2^2 \left(1 - \frac{Q^2}{2p_\nu \cdot p_e} \right)^2 - g_1 g_2 m_e^2 \frac{Q^2}{2(p_\nu \cdot p_e)^2} \right]. \quad (1.9)$$

The quantities g_1 and g_2 depend on the flavour of the neutrino and related to the vector and axial couplings, g_V and g_A . They are:

$$g_1^{\nu_e} = \frac{1}{2} + \sin^2 \vartheta_W, \quad g_2^{\nu_e} = \sin^2 \vartheta_W \quad (1.10)$$

$$g_1^{\nu_{\mu,\tau}} = -\frac{1}{2} + \sin^2 \vartheta_W, \quad g_2^{\nu_{\mu,\tau}} = \sin^2 \vartheta_W. \quad (1.11)$$

The differential cross-section as a function of the electron scattering angle in the laboratory frame is

$$\begin{aligned} \frac{d\sigma}{d\cos\theta} = \sigma_0 \frac{4E_\nu^2(m_e + E_\nu)^2 \cos\theta}{[(m_e + E_\nu)^2 - E_\nu^2 \cos^2\theta]^2} & \left[g_1^2 + g_2^2 \left(1 - \frac{2m_e E_\nu \cos^2\theta}{(m_e + E_\nu)^2 - E_\nu^2 \cos^2\theta} \right)^2 \right. \\ & \left. - g_1 g_2 \frac{2m_e^2 \cos^2\theta}{(m_e + E_\nu)^2 - E_\nu^2 \cos^2\theta} \right], \end{aligned} \quad (1.12)$$

where

$$\sigma_0 = \frac{2G_F^2 m_e^2}{\pi}. \quad (1.13)$$

For what concern the experiments, neutrino interactions with nucleons are easier to study thanks to the much larger cross-section and a more diverse range of processes, despite being less straightforward

¹In terms of Feynman diagrams, the t -channel diagram is replaced by the s -channel diagram.

to deal with theoretically. In general, these processes can be categorised according to the momentum transfer. At small Q^2 , elastic interactions dominate and may be brought about by both charged and neutral currents. When this occurs via neutral currents, all flavour of neutrinos and anti-neutrinos can scatter off both neutrons and protons in what is referred to as “NC elastic” scattering. The process is:

$$\nu_l + N \rightarrow \nu_l + N, \bar{\nu}_l + N \rightarrow \bar{\nu}_l + N, \quad (1.14)$$

Once neutrinos acquire sufficient energy they can also undergo the analogous charged current interactions, called “quasi-elastic”, due to the fact that the recoiling nucleon changes its charge and mass transfer occurs. The processes are

$$\nu_l + n \rightarrow p + l^- \quad (1.15)$$

$$\bar{\nu}_l + p \rightarrow n + l^+, \quad (1.16)$$

with $l = e, \mu, \tau$. For the muonic neutrino with energy below one GeV, the CCQE is the dominant interaction, event though the cross-section plateaus at higher energies, as the available Q^2 increases: it becomes increasingly unlikely for the nucleon to remain intact.

The physics behind the CC quasi-elastic processes is more complicated. The differential cross-section for the scattering in the laboratory frame is given by

$$\frac{d\sigma_{CC}}{dQ^2} = \frac{G_F^2 |V_{ud}|^2 m_N^4}{8\pi(p_\nu \cdot p_N)^2} \left[A(Q^2) \pm B(Q^2) \frac{s-u}{m_N^2} + C(Q^2) \frac{(s-u)^2}{m_N^4} \right], \quad (1.17)$$

where the plus sign refers to the $N = n$ interactions, while the minus sign to $N = p$.

$$\frac{d\sigma_{CC}}{d\cos\theta} = -\frac{G_F^2 |V_{ud}|^2 m_N^2}{4\pi} \frac{p_l}{E_\nu} \left[A(Q^2) \pm B(Q^2) \frac{s-u}{m_N^2} + C(Q^2) \frac{(s-u)^2}{m_N^4} \right], \quad (1.18)$$

The functions $A(Q^2)$, $B(Q^2)$, and $C(Q^2)$ depends on the nucleon form-factors in the following way:

$$A = \frac{m_l^2 + Q^2}{m_N^2} \left\{ \left(1 + \frac{Q^2}{4m_N^2} \right) G_A^2 - \left(1 - \frac{Q^2}{4m_N^2} \right) \left(F_1^2 - \frac{Q^2}{4m_N^2} F_2^2 \right) + \frac{Q^2}{m_N^2} F_1 F_2 - \frac{m_l^2}{4m_N^2} \left[(F_1 + F_2)^2 + (G_A + 2G_P)^2 - \frac{1}{4} \left(1 + \frac{Q^2}{4m_N^2} \right) G_P^2 \right] \right\} \quad (1.19)$$

$$B = \frac{Q^2}{m_N^2} G_A (F_1 + F_2) \quad (1.20)$$

$$C = \frac{1}{4} (G_A^2 + F_1^2 + \frac{Q^2}{4m_N^2} F_2^2). \quad (1.21)$$

The form factors $F_1(Q^2)$, $F_2(Q^2)$, $G_A(Q^2)$, and $G_P(Q^2)$ are called, respectively, *Dirac*, *Pauli*, *axial*, and *pseudoscalar* weak charged-current form factors of the nucleon. These funtions of Q^2 describe the spatial distributions of electric charge and current inside the nucleon and thus are intimately related to its internal structure.

CCQE interactions are particularly important to neutrino physics for mainly two reasons:

- measurements of the differential cross-section in Eq. 1.17 give information on the nucleon form-factors, which are difficult to measure;

- their nature as two-body interactions enable the kinematics to be completely reconstructed, and hence the initial neutrino energy determined which is critical for measuring the oscillation parameters.

In fact, if the target nucleon is at rest, at least compared to the neutrino energy, then this can be calculated as:

$$E_\nu = \frac{m_n E_l + \frac{1}{2}(m_p^2 - m_n^2 - m_l^2)}{m_n - E_l + p_l \cos \theta_l}, \quad (1.22)$$

where the measurement of the momentum, p_l and the angle with respect to the neutrino, θ_l , of the outgoing charged lepton are only required.

Similar calculations can be made for the NCQE scatterings. The cross-sections have the same form as the CC cross-sections in Eq. 1.17 and 1.18, without the mixing term $|V_{ud}|^2$ and with the proper nucleon form factors. Since the values of the electromagnetic form factors, F_1 and F_2 , are reasonably well known and the part in Eq. 1.19 containing G_P can be often neglected, thanks to the different mass magnitudes of leptons and nucleons, the axial form factor, G_A , can be determined through measurements of the charged-current quasielastic scattering processes. On the contrary, measurements of the neutral-current elastic scattering cross-section give information on the *strange* form factors of the nucleon, whose main contribute comes from the strange quark.

The low Q^2 region also presents an inelastic scattering contribution mostly affected by resonance production, where the nucleon is excited into a baryonic resonance before decaying. At high Q^2 , inelastic scattering is dominated by deep inelastic scattering (DIS), because the neutrino can scatter directly off a constituent quark, fragmenting the original nucleon. In between these extreme scenarios, an additional contribution comes from interactions where the hadronic system is neither completely fragmented nor forms a recognisable resonance. These interactions are referred to as “shallow inelastic scattering”, and there is no clear model for dealing with them.

Chapter 2

Experimental techniques for neutrino detections

Being electrically neutral and uncoloured particles, neutrinos can only interact through weak interactions. For this reason, coupled with the small cross-sections typical of the weak force, the study of neutrino results in a challenging task. Direct observation is unfeasible, thus detection must rely on weak interactions with matter, where their SU(2) charged counterparts are either produced or scattered, by CC or NC interactions respectively. The physics is mediated by the lagrangians in Eq. 1.2 and 1.3.

Large active volumes have to be employed, such that a significant number of neutrino can be considered and interaction probability is thus increased. These apparatus are often built underground to shield the detector from cosmic rays and other background radiation. Apart from providing matter to interact with, at the same time these volumes must be capable of detecting the scattered charged leptons. Many are the materials or substances that can be used, like chlorine, gallium, solid or liquid scintillators.

One of the most promising techniques is to combine liquid argon with time projection chambers. As with most other liquefied noble gases, argon has a high scintillation light yield (ca 51 photons/keV[arXiv:1004.0373]), is transparent to its own scintillation light, and is relatively easy to purify. Compared to xenon, argon is also cheaper and has a distinct scintillation time profile which allows the separation of electronic recoils from nuclear recoils.

A more dated and better-known technology is the *water Cherenkov* method, where the detector is used to record the Cherenkov light produced when the particles pass through tanks full of purified water.

2.1 Water cherenkov

The speed of light in vacuum is a universal constant, c , and it is a physical limit of the propagation of information, as stated by the special theory of Relativity. However, when in a medium, light may

travel at speed significantly less than c . This reduction of speed depends on the relative permittivity, ϵ , of the material in which light is propagating. Because of the non-zero real part of the dielectric constant, the electromagnetic (EM) field is modified and the phase velocity of light changes into

$$v_P = \frac{c}{\sqrt{\epsilon(\lambda)}} = \frac{c}{n(\lambda)}, \quad (2.1)$$

where $n(\lambda) > 1$ is the *refractive index* of the medium and depends on the wavelength (energy) of the wave.

A charged particles moving at a constant velocity in a dielectric medium disrupts the local electromagnetic field, by deforming its molecules and temporarily polarising the material. The dipoles are restored almost instantaneously and thus become impulsive sources of EM waves. If the velocity of the passing particle, $v = \beta c$, is less than the speed of the light in the medium as expressed in Eq. 2.1, i.e. $\beta < 1/n$, then the total energy flux of the excited field is zero and EM waves are not irradiated. On the contrary, if $\beta > 1/n$, the perturbation left by the passage of the particle is such that the energy is released coherently. The result is that the field is different from zero in a cone coaxial with respect to the direction of the charged particle, whose direction is opposite to the particle motion. As far as the photons are concerned, these are emitted coherently to a fixed angle with respect to the particle motion. With the help of Fig. ??, it is easy to find that:

$$\sin \alpha = \frac{1}{\beta n} \quad (2.2)$$

$$\cos \theta = \frac{1}{\beta n}. \quad (2.3)$$

where α is the apex angle of the cone and θ is the photon angle with respect to the particle direction. For an ultra-relativistic particle, for which $\beta \sim 1$, there is a maximum angle of emission, given by:

$$\cos \theta_{\text{MAX}} = \frac{1}{n}. \quad (2.4)$$

The phenomenon is called *Cherenkov effect*, and it occurs everytime a charged particle passes through a dielectric medium at a speed:

$$\beta > \frac{1}{n}. \quad (2.5)$$

According to the theory of electromagnetic waves, a charged particle moving uniformly does not irradiate and this proves that the Cherenkov radiation is not related with Bremsstrahlung.

This condition can be expressed in terms of the particle energy, given that $E^2 = p^2 + m^2$ and $\beta = p/E$ ¹. The threshold becomes:

$$\frac{E}{m} > \frac{1}{\sqrt{1 - 1/n^2}}, \quad (2.6)$$

with m the mass of the charged particle.

The radiation is emitted in the visible and near visible regions of the EM spectrum, for which $n > 1$. A real medium is always dispersive and radiation is restricted to those frequencies bands for which

¹For this calculation, the convention $c = 1$ is adopted.

$n(\nu) > \frac{1}{\beta}$. In the x-ray region, for instance, $n(\nu)$ is always less than one and radiation is forbidden at this energies, because Eq. 2.5 cannot be satisfied.

Truly, coherent emission of light needs two more conditions to be fulfilled:

- the length of the track of the particle in the medium should be large compared with the wavelength, λ , of the radiation in question, otherwise diffraction effects will become dominant;
- the velocity of the particle must be constant during its passage through the medium, or, to be more specific, the differences in the times for particle to traverse successive λ distances should be small compared with the period $\frac{\lambda}{c}$ of the emitted light.

The number of photons emitted by a charged particle of charge Ze per unit path length and per unit energy interval, or equivalently to λ , of the photons is equal to:

$$\frac{d^2N}{dx d\lambda} = \frac{2\pi\alpha Z^2}{\lambda^2} \left(1 - \frac{1}{\beta^2 n^2(\lambda)}\right). \quad (2.7)$$

This means that the greater part of Cherenkov photons are emitted in the ultraviolet range, because of the proportionality to $1/\lambda^2$.

Cherenkov detectors take advantage of this effect, detecting the light produced by charge particles. A large volume of transparent material, such as water, ice, or liquid scintillator, can be surrounded by lightsensitive detectors in order to capture the Cherenkov radiation. This technique is largely used in neutrino detection, since they cannot be detected directly: the charged lepton, yeilded in CC or NC interactions, is observed. From the light collected, it is possibile to reconstruct information on the interaction, such as the velocity of the charged particle, which is somehow related to the energy of the incident neutrino, or the position of the interaction vertex. If the charged lepton drop under the Cherenkov threshold, the light is emitted in the shape of a ring, which further data can be inferred from. Not every neutrino energy allows the production of a charged lepton², but only MeV-scale neutrinos can be observed in a Cherenkov detector.

2.2 Gadolinium neutron capture

Current multi-kiloton scale water Cherenkov detectors, like Super-Kamiokande (SK), have provided many clues in the experimental understanding of the neutrino, be it originated in solar, atmospheric, or accelerator reactions. However, in spite of the large lifetime of the experiment, some analyses are still limited by statistical uncertainty, and would benefit from increasing exposure. Other analyses suffer from background contamination, as in the case of the supernova relic neutrinos (SRN) search, and would benefit more from the development of new background suppression techniques. This hindrance can be overcome by studying the yield of neutrons in neutrino interactions, such as the *inverse beta decay* (the

²For instance, the CCQE process $\bar{\nu}_e + p \rightarrow n + e^+$ has a energy threshold of 1.81 MeV and the interaction $\nu_\mu + n \rightarrow p + \mu^-$ has the threshold of 110.16 MeV, because of the muon mass.

antineutrino CCQE scattering). It would allow a handle on antineutrinos rate, and possibly a method of background reduction for other studies.

Since neutrons are chargeless, they cannot interact with matter by means of the Coulomb force, which dominates the energy loss mechanisms for charged particles, described by the Bethe formula. Neutrons can interact with nuclei in various way, depending on the energy:

- elastic and inelastic scattering;
- transmutation;
- neutron activation;
- spallation reaction;
- neutron-induced fission;

As a result of the interaction, the neutron may either be absorbed, or change its energy and direction significantly. In this way the average energy of a neutron beam can be completely or partly reduced up to thermal energies, close to 0.025 eV. In this range of energy, the neutron presents a different and often much larger effective neutron absorption cross-section for a given nuclide, compared to, for instance, fast neutrons, hence *thermalisation* can result in a *neutron activation* process. This occurs when atomic nuclei capture free thermal neutrons, creating heavier nuclei, often in an excited state. The excited nucleus decays almost instantaneously emitting usually gamma rays.

The neutron energy distribution is adopted to the Maxwellian distribution known for thermal motion. The time required by the thermalisation of neutrons follows an exponential, and the time constant is largely studied, [ref needed], amongst all the thermalisation in water. It was found that neutron thermalisation in water has a time constant of $5\mu\text{s}$ [fujino, sumita, shiba]. Neutrons can be captured by either the hydrogen or the oxygen. Free neutron will capture on a hydrogen nucleus, releasing a 2.2 MeV gamma. In SK, for instance, this gamma results in about seven photo-electrons, and thus only detectable with $\simeq 20\%$ efficiency.

Gadolinium-157 has the highest thermal neutron capture cross-section among any stable nuclides: 259,000 barns. Dissolving gadolinium compounds in water could considerably increase the neutron capture probability. The neutron in water thermalises quickly and can thus be captured by a Gd nucleus with a probability of 90 %. Upon capturing a neutron the Gd emits 3-4 gamma rays having a total energy of about 8 MeV. The time and spatial correlation of the positron and neutron capture events ($20\ \mu\text{s}$ and 4 cm) can significantly reduce the backgrounds, and hence enhance the neutrino signal events. Even moderately energetic neutrons ranging from tens to hundreds of MeV will quickly lose energy by collisions with free protons and oxygen nuclei in water. Once thermalised, the neutrons undergo radiative capture, combining with a nearby nucleus to produce a more tightly bound final state, with excess energy released in a gamma-ray () cascade. Gd-doped water enhances the capture cross-section

compared to pure water (49,000 barns compared with 0.3 barns on a free proton) and, since the cascade happens at higher energies (8 MeV vs 2.2 MeV), it produces enough optical light to be reliably detected in a large target volume.

2.3 Neutrino Production

Numerous are the neutrino sources at the reach of neutrino experiments. Neutrinos are produced in CC interactions, which can happen in nuclear reaction, as for *solar* or *reactor* neutrinos, or in cosmic rays impacts with the Earth's atmosphere, conveying energetic *atmospheric* neutrinos.

Artificial neutrinos are also yielded in high-energy proton accelerators. Accelerator neutrino beams are fundamental instrumental discovery tools in particle physics, in that more control less variables are involved. Neutrino beams are derived from the decays of charged π and K mesons, which in turn are created from proton beams striking thick nuclear targets. The precise selection and manipulation of the π/K beam control the energy spectrum and type of neutrino beam.

The π^\pm mesons have a mass of 139.6 MeV and a mean lifetime of 2.6×10^{-8} s. The primary decay mode of a pion, with a branching fraction of 99.9877 %, is a leptonic decay into a muon and a muon neutrino:

$$\pi^+ \rightarrow \mu^+ + \nu_\mu \quad (2.8)$$

$$\pi^- \rightarrow \mu^- + \bar{\nu}_\mu \quad (2.9)$$

The second most common decay mode of a pion, is the leptonic decay into an electron and the corresponding neutrino, $\pi^\pm \rightarrow \nu_e + e$. In spite of the considerable differences in the space momentum, this process is suppressed with respect to the muonic one. This effect is called *helicity suppression* and is due to the great mass of the muon ($m_\mu = 105.658$ MeV) compared to the electron's ($m_e = 0.510$ MeV); this results in a stronger helicity-chirality correspondence for the electron rather than for the muon. Given that the π mesons are spinless, neutrinos are left-handed, and antineutrinos are right-handed, the muonic channel is preferred because of spin and linear momentum preservation. The suppression of the electronic decay mode with respect to the muonic one is given approximately within radiative corrections by the ratio:

$$R_\pi = \left(\frac{m_e}{m_\mu} \right)^2 \left(\frac{m_\pi^2 - m_e^2}{m_\pi^2 - m_\mu^2} \right) = 1.283 \times 10^{-4} \quad (2.10)$$

The measured branching ratio of the electronic decay is indeed $(1.23 \pm 0.02) \times 10^{-4}$.

As far as the charged K meson is concerned, it mainly decays in a muon and its corresponsive neutrino, with a branching ratio of 63.55 %:

Tab. 2.1: Decay mode for a charged kaon, K^\pm , sorted by branching ration (in percent).

$\mu^\pm + \nu_\mu^{(-)}$	65.55 ± 0.11
$\pi^\pm + \pi^0$	20.66 ± 0.08
$\pi^+ + \pi^\pm + \pi^-$	5.59 ± 0.04
$\pi^0 + e^\pm + \nu_e^{(-)}$	5.07 ± 0.04
$\pi^0 + \mu^\pm + \nu_\mu^{(-)}$	3.35 ± 0.03
$\pi^\pm + \pi^0 + \pi^0$	1.76 ± 0.02

$$K^+ \rightarrow \mu^+ + \nu_\mu \quad (2.11)$$

$$K^- \rightarrow \mu^- + \bar{\nu}_\mu \quad (2.12)$$

The second most frequent decay (20.66 %) is the decay into two pions, $K^\pm \rightarrow \pi^0 + \pi^\pm$. Other decays have a branching ratio of 5 % or less and are listed in table Tab. 2.1. On the contrary, the decays of the neutral kaon produce neutrino in few cases. Because of the oscillation phenomenon given by the mixing between K^0 and \bar{K}^0 , the neutral kaon has two manifestations, the short kaon K_S and the long kaon K_L , named after their lifetimes. While the K -short decays only in two pions ($2\pi^0$ or $\pi^+ + \pi^-$), the K -long has a wider variety of final state combination, all of them involving three particles. Among these, neutrinos are produced in the processes:

$$K_L^0 \rightarrow \pi^\pm + \mu^\mp + \nu_\mu^{(-)} \quad (2.13)$$

$$K_L^0 \rightarrow \pi^\pm + e^\mp + \nu_e^{(-)} \quad (2.14)$$

Neutrinos are also produced by the decay of muons. Muons are unstable elementary particles and decay via the weak interaction. The dominant decay mode, called *Michel decay*, is also the simplest possible: because lepton numbers must be conserved, one of the product neutrinos of muon decay must be a muonic neutrino and the other an electronic antineutrino, along with an electron, because of the charge preservation. Vice versa, an antimuon decay produces the corresponding antiparticles. These two decays are:

$$\mu^- \rightarrow e^- + \bar{\nu}_e + \nu_\mu \quad (2.15)$$

$$\mu^+ \rightarrow e^+ + \nu_e + \bar{\nu}_\mu \quad (2.16)$$

The neutrino source provided by the muon decay, is more of a nuisance background, because of the long lifetime, which give rise to electronic component in neutrino spectrum. Usually a beam absorbed is located at the end of the decay region of an accelerator line, to stop the hadronic and muonic component of the beam, and only an almost pure neutrino beam pointing towards te.

2.4 Liquid argon time projection chamber

Chapter 3

Continuous gadolinium measurement

In the next phase of the Super-Kamiokande experiment, a gadolinium salt compound $\text{Gd}_2(\text{SO}_4)_3$ will be added to the detector [], which will improve the ability of the detector to identify neutrons. Neutrons are emitted in inverse beta decay (IBD) process, $\bar{\nu}_e + p \rightarrow e^+ + n$. The current technique to tag neutrons in SK is by detecting capture on hydrogen nuclei. Capture of a thermal neutron on hydrogen has a cross section of 332.6 ± 0.7 b, characteristic time of $\sim 200 \mu\text{s}$ in water, with the release of 2.2 MeV gammas. After the prompt Cherenkov radiation from the charged lepton, the secondary signal from an electron, compton-scattered by the 2.2 MeV photon, is looked for in a long time window. However, in water what matters are the electrons Compton-scattered above the Cerenkov threshold by relatively hard gammas. The detectable light following neutron capture on Gd (in thin foils) in possible discrete counters was carefully simulated for the SNO heavy water Cerenkov detector. The equivalent single electron energy was found to peak at about 5 MeV, and range over 3–8 MeV. This spread reflects the intrinsic variation in the gamma cascades and the detector energy resolution (the simulation had 5 photoelectrons per MeV of electron energy, compared to 6 in SK-I) [?]. The energy threshold for SK is 5 MeV, and the search of hydrogen-tagged neutrons is not efficient (20%). a long time window in which to look for the hydrogen signal, Capture on gadolinium has a cross section of 49×10^3 b, which de-excites emitting a ~ 8 MeV gamma-ray cascade. By adding 0.2 % by mass of the Gd salt as $\text{Gd}_2(\text{SO}_4)_3$, the characteristic time of capture is $\sim 30 \mu\text{s}$ and an efficiency of 90 % can be achieved. The isotopes ^{155}Gd and ^{157}Gd present very high cross-sections to thermal neutron capture, respectively 6.074×10^4 b and 2.537×10^5 b. Hydrogen alone has a cross section of 3.321×10^{-1} b.

One of the main motivation to detect neutrons is to be able to detect relic supernova neutrinos, also known as Diffuse Supernova Neutrino Background (DSNB), produced from all previous core-collapse supernova explosions in the Universe. This measurement will provide very important information on, for example, the mean energy spectrum of core collapse supernovae and the star formation rate of the universe. This measurement is largely affected by irreducible backgrounds, like invisible muon decay at low energies—muons below Cherenkov threshold that decay into electrons—and at high energies by atmospheric neutrinos. The lower energy threshold is defined by our ability to remove spallation

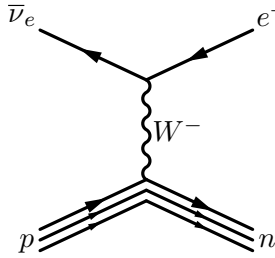


Fig. 3.1: Inverse beta decay.

events and solar neutrinos, that can be excluded effectively with neutron tagging. The energy of these neutrinos should be around a few tens of MeV. The largest cross section in this search corresponds to IBD, which is two orders of magnitude larger than ν_e elastic scattering. The predictions provide with several limits but although SK has the best world limit, DSNB has not been detected yet. However, if we could detect neutrons efficiently, these backgrounds could be reduced significantly and thus, making the detection of the DSNB possible for the first time.

Another motivation is searches of galactic supernova burst. When a massive star at the end of its life collapses to a neutron star, it radiates almost all of its binding energy in the form of neutrinos, most of which have energies in the range 10 to 30 MeV, and are emitted over a timescale of several tens of seconds. These neutrinos are released just after core collapse, whereas the photon signal may take hours or days to emerge from the stellar envelope. SK will acquire a huge number of neutrino events if the supernova is inside out galaxy, providing much information about early stages of the core-collapse process, its spectrum and time profile. Stars that are at the onset of their collapse, just after carbon ignition, will release most of its energy through neutrinos. During the silicon burning stage, the neutrino luminosity is eight orders of magnitude less than in the peak at core-collapse, but while the later lasts just a few seconds, the Si burning phase takes several days. During the Si burning phase roughly 1% of the total energy of core-collapse are emitted through “pre-supernova” neutrinos with a monotonically increasing rate.

Improved neutron tagging will also be helpful to understand atmospheric and accelerator neutrino interactions and final states. Also the separation of neutrino and antineutrino at the GeV scale will benefit from neutron tagging. Finally, the background in proton decay searches can be reduced, since it requires no neutrons to appear in the final state.

3.1 Gadolinium sulfate

In the original proposal by John Beacom and Mark Vagins, gadolinium trichloride $GdCl_3$ was proposed, but the current full-scale plan has steered on gadolinium sulfate $Gd_2(SO_4)_3$ as the salt of choice (other candidate could be gadolinium nitrate $Gd(NO_3)_3$). There are a few requirements which a Gd compound must meet in order to become a good candidate for a full scale test. The compound must be water soluble, and it should not be too difficult to dissolve large amounts. The above three candidates

can all be dissolved fairly easily, with the GdCl_3 and $\text{Gd}(\text{NO}_3)_3$ only needing stirring to fully dissolve, while the $\text{Gd}_2(\text{SO}_4)_3$, can be forced into solution with the addition of a small amount of sulfuric acid, about 380 ml of acid for 28 kg of $\text{Gd}_2(\text{SO}_4)_3$ in 14 tons of water (test done at EGADS). So, this solubility requirement does not immediately rule out any of these three compounds. Next, if the compound is to be used inside a very large water Cherenkov detector, such as SK, it must be safe for the detectors components and tank, and it should be a non-toxic chemical, so it may be easily put into existing detectors. While none of the above salts are toxic, they do have very different corrosive properties, due to the different anions of the molecule. The nitrate and the sulfate turn out to be non-corrosive, and do not seem to affect detectors components much, if at all. An extensive soak test study was carried out in Japan, with each of the 31 different materials inside the SK detector being soaked in both pure water and $\text{Gd}_2(\text{SO}_4)_3$ solution. Only the rubber used for the PMT pressure housing showed any difference between the pure water and the $\text{Gd}_2(\text{SO}_4)_3$ solution, with further studies showing the rubber is unaffected by the Gd solution, if the temperature is kept below 15 °C, which it is in the case of SK. However, the chloride is corrosive, so for this reason the GdCl_3 has been ruled out as a full scale test candidate. Last the Gd compound solution must maintain a high level of optical transparency, so that light can be seen from the opposite side of the detector. Although the GdCl_3 has fairly good optical properties, it has been ruled out by the above. $\text{Gd}(\text{NO}_3)_3$ is opaque in the UV region of the electromagnetic (EM) spectrum, for wavelengths less than 350 nm, and this unfortunately is where a large fraction of Cherenkov light is detected in SK PMTs, so it cannot be a good full scale test candidate either. This leaves $\text{Gd}_2(\text{SO}_4)_3$, and it turns out to have good transparency in the UV and optical regions of the EM spectrum, leaving it as the best candidate for the EGADS test facility. This is in fact the choice that has been made by the EGADS group, and the remaining studies described in this paper have been done using, or under the assumption that, $\text{Gd}_2(\text{SO}_4)_3$ will be used. One last exceptionally nice quality about this compound is today it costs only 5 US dollars per kilogram, meaning it would only be about 500,000 US dollars to dope SK [11], a price which is on the scale of such a major experiment. [?].

3.2 Gadolinium purity

3.3 Gadolinium concentration

The concentration of Gd in water affects the efficiency and timing of neutron captures, antineutrino measurements depends on this. It is fundamental to measure the concentration regularly, as this can change in time inside the tank. On such a large scale, it is not a trivial task to predict temperature and flow dependency of the dissolved Gd. At the moment, the Evaluating Gadolinium's Action on Detector Systems (EGADS) keeps track of the Gd concentration with a Zeeman atomic absorption spectrometer, located near the experiment. Water samples are collected from the EGADS tank, diluted and atomised inside the AAS machine. The amount of Gd is then compared to known samples of Gd loaded water to

determine the concentration.

We propose an alternative method, which still uses atomic absorption lines of Gd, but in solution in water. Gadolinium presents strong emission/absorption lines in the UV region [?]. Using a UV source and a spectrometer it would be possible to measure the absorption by gadolinium dissolved in water. The absorption is directly proportional to the amount of gadolinium and therefore the concentration, where absorption is defined as

$$\mathcal{A}(x) = \log_{10} \frac{I_0(x)}{I(x)}, \quad (3.1)$$

where $I_0(x)$ is the reference intensity of the light source at wavelength x and $I(x)$ is the measured intensity at the same wavelength. The reference intensity would be using a pure water sample.

Using two absorption peaks the measurement could be improved by taking the difference of the absorption, as any effect which is wavelength independent is removed.

$$\Delta\mathcal{A} = \mathcal{A}(x_1) - \mathcal{A}(x_2) = \log_{10} \frac{I_0(x_1)}{I(x_1)} - \log_{10} \frac{I_0(x_2)}{I(x_2)}, \quad (3.2)$$

The automated Gadolinium absorbance detector (GAD) is progressing well. The first prototype based on a 10 cm cell for 0.2% Gadolinium sulphate doping achieved a 3% concentration measurement resolution (1% neutron capture efficiency) at the target concentration in comparison to the 3.5% currently achieved via a manual mass spectrometer method.

This device was intended for deployment in EGADS in Japan but the Gadolinium sulphate concentration was changed to 0.02% in preparation for Super-K phase 1 loading. Therefore work progressed to building the version 2 prototype of GAD for sensitivity to 0.02%, by increasing the volume to ≈ 1 meter.

This prototype has been successfully built and tested and shown a concentration measurement resolution of 1% at both 0.02% and 0.2% doping. Figure ?? shows the new system and Figure ?? shows the performance of the new system.

Chapter 4

Neutron calibration with a californium source

To measure neutron tagging efficiency, an americium-beryllium (Am-Be) source is placed inside a bismuth germanite (BGO) crystal scintillator and the whole device is usually deployed at the centre of the water Cherenkov detector. The americium-241 goes through α decay with a half-life of 432.6 y. [100% ?] The α particle is captured by the ^9Be nuclei to become $^{12}\text{C}^*$ with the emission of a neutron. The carbon de-excites to the ground state with sometimes the emission of a 4.43 MeV photon. The gamma ray is promptly captured by the BGO crystal, and the scintillation light triggers the detector. The neutron thermalises in the water with an average time of roughly 200 μs , before begin captured on a hydrogen nucleus with the release of a 2.2 MeV photon. Neutron tagging efficiency on hydrogen in SK was measured to be $(19.0 \pm 0.2)\%$, using a unbinned maximum likelihood fitting []. Neutrons released by beryllium have an energy ranging from 2-10 MeV, much less than the average neutron energy following atmospheric neutrino interactions. Thus, we can make the assumption that the location of the Am-Be apparatus is roughly the same as the neutron capture vertex.

Another possible source for neutron calibration is californium-252, which undergoes α -emissions (96.91%) and spontaneous fission (SF) (3.09%). With a half-life of 2.645 y, a ^{252}Cf source has a higher activity compared to an Am-Be source with the same number of nucleons. Furthermore, the SF process emits an average of 3.75 neutrons per fission and an average of 10.3 photons having a total energy of 8.2 Mev. As for the case of Am-Be, the photons can be collected by a scintillating material to tag the emission of neutrons. After this trigger signal, multiple neutron captures on hydrogen are expected, separated by short intervals in time. The yield of multiple neutrons is another advantage of ^{252}Cf that the SNO collaboration exploited to develop a method, called *Time Series Analysis* method that uses multiplicity and time intervals between the detected events to find the neutron detection efficiency, the neutron mean life inside the detector, and activity from non-fission events. The fast-neutron and photon energy spectra are shown in 4.1: the neutrons are emitted with a most-probable energy of 0.7 MeV and

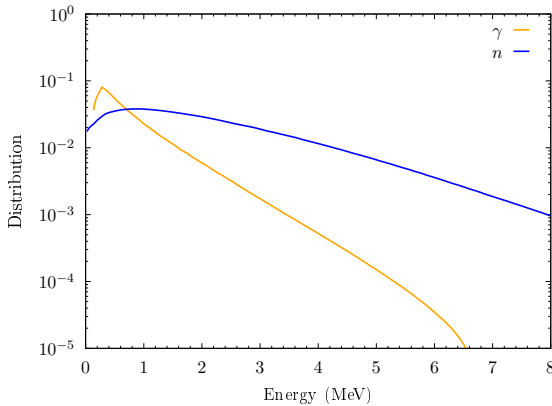


Fig. 4.1: Normalised energy distribution of neutron and photons emitted by SF events of a ^{252}Cf source [1, 2].

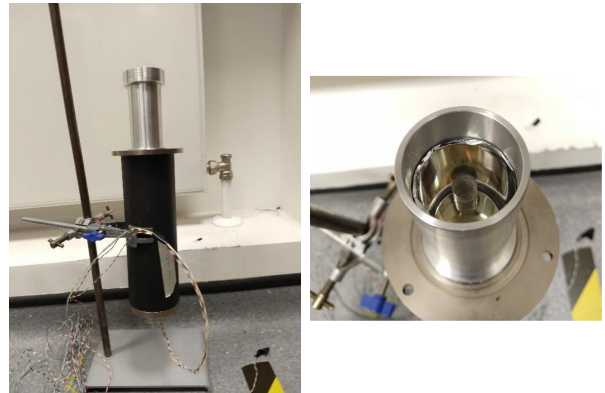


Fig. 4.2: Setup used to test the californium source.

an average energy of 2.1 MeV.

A ^{252}Cf source was purchased by QMUL with an activity of 4.3 kBq, measured on the 28th of July, 2017. The californium is encapsulated in a double hull stainless steel cylinder, 9.5 mm in diameter and 37.5 mm high. The source is tested in a simple calibration device (see Fig. 4.2), which consists of a cylindrical plastic scintillator (EJ-200), coated with mylar to contain optical photons, and optically coupled to a ET Enterprise 9902B series PMT. A hole, coaxial to the plastic cylinder, allows to place the source in the middle of the scintillator. The cylinder is 3 in in length and 1.5 in in diameter. With this setup, the rate of photons emitted by the ^{252}Cf source can be measured; we used a Struck SIS3316 14-bit VME digitiser to count the number of photon triggers from the PMT and a daisy-chain of NIM amplifier, threshold, and discriminator is used before the digitiser to optimise the signal. Without the source inside the scintillator, an event rate of 1.633 Hz was measured, whereas with the source inside the rate increases to 41.395 Hz. The distributions of the PMT peaks collected by the digitiser are shown in Fig. 4.3. A predicted activity of 3.1 kBq is expected on the day when the measurement was taken—446 days after the activity measurement—which translates to a SF rate of 96.46 Hz. The SF tagging efficiency with this setup is therefore around 41 %.

We performed a GEANT4 simulation of the setup, with the aim of optimising the calibration device. An ideal calibration device would absorb all the photons converting them into visible light without affect the neutrons. The plot in Fig. 4.4 shows the correct implementation of the scintillator and PMT efficiencies, as there is good agreement with the MC distribution and the expected optical photon spectrum. The scintillating volume is therefore varied in the simulation to study the performance of the device. Bismuth germanate oxide (BGO) crystal and a generic vinyltoluene plastic are studied as scintillating materials. The size of the scintillator is also varied and shapes of a cube and a cylinder with equal diameter and height are tested. The simulation keeps track of the energy deposited in the scintillator and the number of neutrons escaping the device. The result is shown in Fig. 4.5. Unsurprisingly, the BGO crystal performs better than the plastic scintillator, with the optimal volume

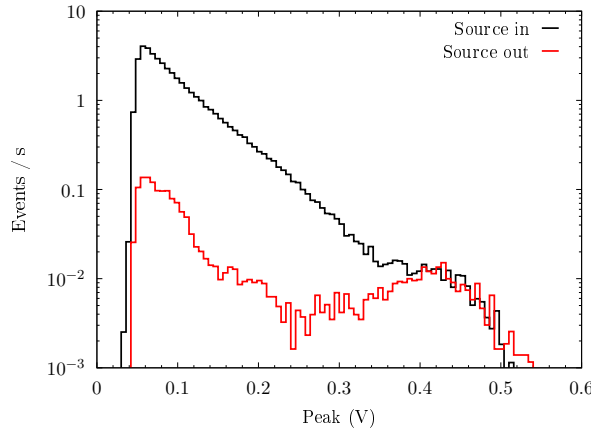


Fig. 4.3: Distribution of PMT peaks measured with source inside (black) and source removed from the scintillator (red).

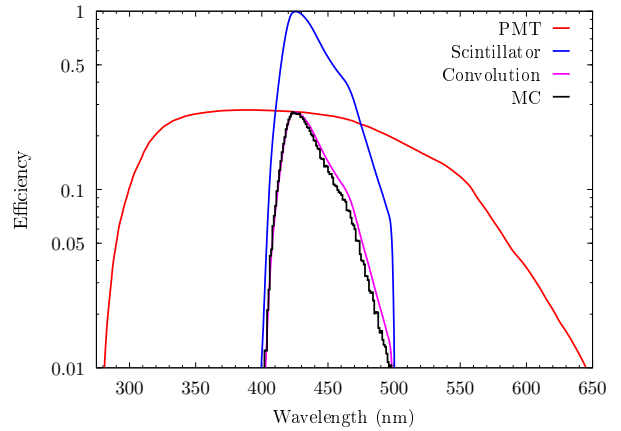


Fig. 4.4: Plot showing PMT quantum efficiency (red), the scintillator yield (blue), their convolution (magenta) and the distributions of photon collected by the PMT in the GEANT4 simulation of optical photons (black).

being a cube with 12 cm sides. The hydrogen in the plastic thermalises neutrons, which can have an impact on the thermalisation time in a water Cherenkov detector.

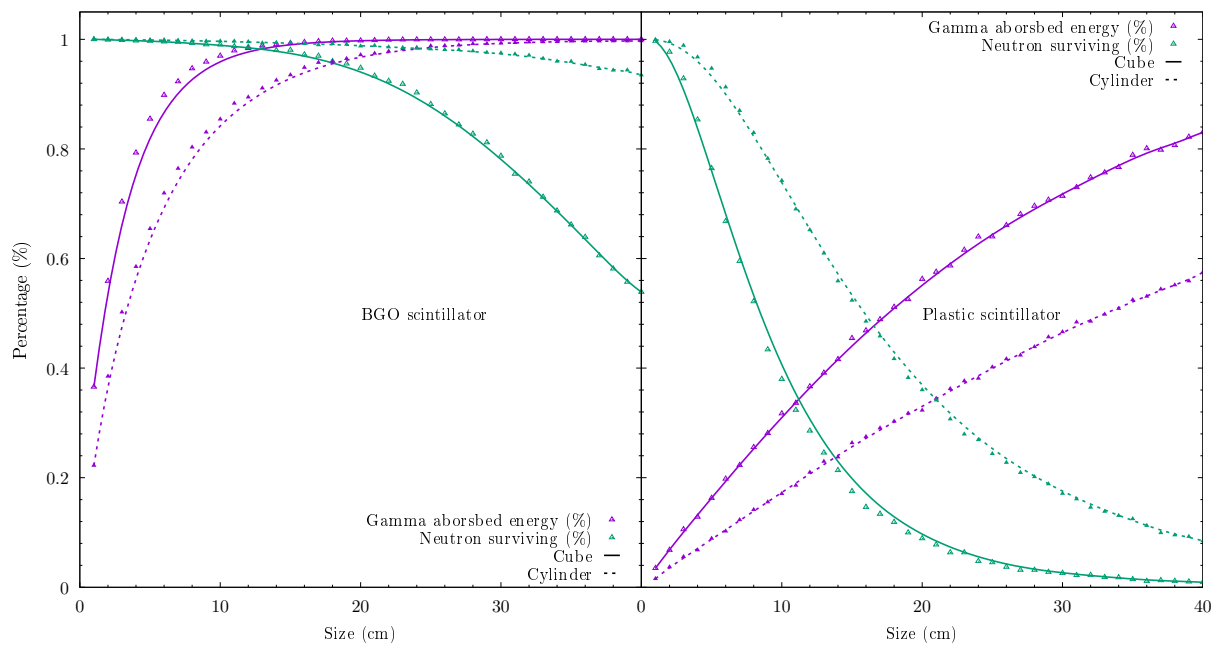


Fig. 4.5: Result of the GEANT4 simulation, showing the performance of different scintillators. Two shapes are tested: a cube (solid lines) and a cylinder with equal diameter and height (dashed lines). The percentage of energy absorbed by the scintillator (purple) and the percentage of neutrons escaping the scintillators (green) are estimated for every simulation. Left: BGO is used as scintillating material. Right: a generic vinyltoulene plastic is used.

Chapter 5

Hyper-Kamiokande sensitivity to δ_{CP}

The violation of the CP symmetry is a well-known process in the quark sector of the standard model (SM), giving clear evidence that the Cabibbo-Kobayashi-Maskawa matrix is complex. As three generations exist, an entirely analogous phenomenon is expected to arise in the lepton sector. The leptonic mass mixing matrix, the Pontecorvo–Maki–Nakagawa–Sakata (PMNS) matrix, is usually parameterised as

$$U = \begin{pmatrix} 1 & 0 & 0 \\ 0 & c_{23} & s_{23} \\ 0 & -s_{23} & c_{23} \end{pmatrix} \begin{pmatrix} c_{13} & 0 & s_{13}e^{-i\delta_{\text{CP}}} \\ 0 & 1 & 0 \\ -s_{13}e^{i\delta_{\text{CP}}} & 0 & c_{13} \end{pmatrix} \begin{pmatrix} c_{12} & s_{12} & 0 \\ -s_{12} & c_{12} & 0 \\ 0 & 0 & 1 \end{pmatrix} \begin{pmatrix} 1 & 0 & 0 \\ 0 & e^{i\gamma_1} & 0 \\ 0 & 0 & e^{i\gamma_2} \end{pmatrix} \quad (5.1)$$

where $c_{ij} \equiv \cos \theta_{ij}$ and $s_{ij} \equiv \sin \theta_{ij}$. The angle δ_{CP} is the phase responsible for CP violation, whereas the additional phases γ_1 and γ_2 bring about CP violation if the neutrinos are Majorana.

C and CP violation are some of the conditions required in order to generate an asymmetry between matter and antimatter particles, together with baryon number violation and interactions out of thermal equilibrium [3]. The amount of CP violation in the quark sector is not enough to describe the observed baryon asymmetry within the SM. An asymmetry in the lepton sector, however, could be translated into baryogenesis, via non-perturbative sphaleronic processes [4]. This process, called *leptogenesis*, would be allowed by the addition of right-handed Majorana neutrinos to the SM, which can violate lepton number. This elegant solution to explain the baryon asymmetry is a strong motivation for searches of signals of CP violation in the lepton sector.

5.1 CP violation in neutrino oscillations

The best probe to discovery CP violation is neutrino oscillation, being a purely weak process in which CP-conjugate processes can be easily studied. The PMNS matrix relates flavour states $\alpha = e, \mu, \tau$ with mass eigenstates $i = 1, 2, 3$ as $|\nu_\alpha\rangle = \sum_i U_{\alpha i}^* |\nu_i\rangle$. The probability of flavour oscillation in vacuum is hence computed as

$$P(\nu_\alpha \rightarrow \nu_\beta) \equiv |\langle \nu_\alpha | e^{-i\mathcal{H}t} | \nu_\beta \rangle|^2 = \sum_{ij} U_{i\alpha}^* U_{\beta i} U_{\alpha j} U_{j\beta}^* \exp\left(-i \frac{\Delta m_{ij}^2 L}{2E}\right), \quad (5.2)$$

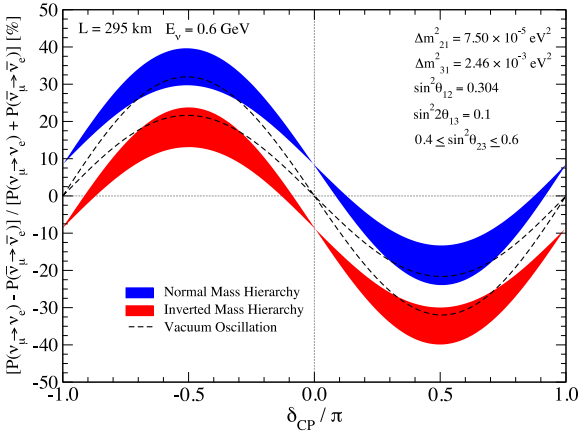


Fig. 5.1: Effect of δ_{CP} on the normalised asymmetry from Eq. 5.3.

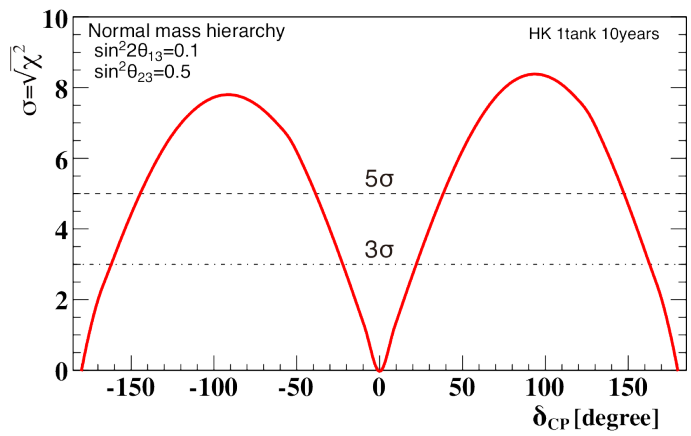


Fig. 5.2: Expected significance to exclude CP conservation, in case of normal hierarchy, where the mass hierarchy is assumed to be known [10].

where \mathcal{H} is the Hamiltonian, $t \simeq L$ and $\Delta m_{ij}^2 = m_i^2 - m_j^2$, and it depends on the physical angles and phases of the PMNS matrix, with the exception of the Majorana phases $\gamma_{1,2}$. The CP-conjugate of a neutrino with negative helicity is an antineutrino with positive helicity, which, in terms of neutrino oscillations, means transforming the $\nu_\alpha \rightarrow \nu_\beta$ oscillation channel into the $\bar{\nu}_\alpha \rightarrow \bar{\nu}_\beta$ channel. The violation of CP in neutrino oscillation can be quantified by the asymmetry in oscillation probabilities between neutrinos and antineutrinos

$$A_{\alpha\beta}^{CP} = P(\nu_\alpha \rightarrow \nu_\beta) - P(\bar{\nu}_\alpha \rightarrow \bar{\nu}_\beta) = 4 \sum_{i>j} \Im[U_{i\alpha}^* U_{\beta i} U_{\alpha j} U_{j\beta}^*] \sin\left(\frac{\Delta m_{ij}^2 L}{2E}\right). \quad (5.3)$$

It follows that CP violation can only be measured in ‘‘appearance’’ channels, as the argument of the imaginary part of Eq. 5.3 is real for $\alpha = \beta$. Furthermore, given the parametrisation in Eq. 5.1, this asymmetry is not measurable if the phase is trivial, *i.e.* $\delta_{CP} = 0$ or $\pm\pi$, or if θ_{13} is vanishing. From a model building point of view, however, a successful leptogenesis requires the parameters to satisfy $|\sin \theta_{13} \sin \delta_{CP}| \gtrsim 0.09$ when the Majorana phases are vanishing [5]. The value of θ_{13} has been measured to be non-zero [6–9] and for this reason it is expected that on-going and future generation neutrino experiments will also constrain the value of δ_{CP} . The effect of the CP-violating phase on the asymmetry of Eq. 5.3 can be appreciated from the plot in Fig. 5.1.

5.2 Hyper-Kamiokande experiment

Hyper-Kamiokande (HK) [10] will be the next-generation water Cherenkov detector, starting taking data from 2027. Similar in concept to its predecessor, Super-Kamiokande (SK), the cylindrical tank of HK will be 72 m high and 68 m in diameter, with a fiducial volume of 188.4 kton, around 8.4 times the fiducial volume of SK. The photo-coverage of the inner detector region will be 40 %, the same of SK, but it translates to roughly forty thousands photomultipliers (PMTs). New PMTs, with twice the quantum efficiency of the previous generation and improved charge and timing resolution, will be employed.

Thanks to incredible statistics and cutting edge resolutions, HK will be capable of a vast variety of physics studies, from accelerator and atmospheric neutrinos to solar and supernova neutrinos. Besides detecting proton decay, the main goal of HK is to measure δ_{CP} and constrain the other oscillation parameters with high precision. This is achievable by studying accelerator neutrinos, and to this end the possibility of installing a second detector in Korea, at the secondary oscillation peak, is being investigated.

HK will be located 295 km away from the target and 2.5° off-axis with respect to the beamline. The neutrino beam is generated by a 30 GeV proton beam colliding on a fixed graphite target; a focusing horn selects positively charged (ν mode) or negatively charged ($\bar{\nu}$ mode) pions, which decay leptonically, to obtain an almost pure muon neutrino or antineutrino beam, peaking at 600 MeV. The accelerator facility at J-PARC will undergo a planned upgrade to increase the beam power up to 1.3 MW, before HK starts operation. The T2K near detector system, comprised of the two modules ND280 and INGRID, will be refurbished and the new Intermediate Water Cherenkov Detector, possibly gadolinium-loaded, will be located around 1 km from the target.

HK will take data for ten years, collecting a total of 2.7×10^{22} Protons On Target, divided between ν and $\bar{\nu}$ beam modes. Assuming $\nu : \bar{\nu} = 1 : 3$ and $\delta_{CP} = 0$, the expected number of fully-contained events in the fiducial volume for the channels $\nu_\mu \rightarrow \nu_e$ and $\bar{\nu}_\mu \rightarrow \bar{\nu}_e$ are respectively 1643 and 15 in ν mode and 206 and 1183 in $\bar{\nu}$ mode, assuming CP conservation. Deviations from these expected numbers could be indication of CP violation. A preliminary study for the HK design report [10], using a different analysis, estimated a significance well-above 5σ after ten years of data taking, as can be seen in Fig. 5.2.

5.3 Sensitivity to δ_{CP}

The sensitivity of HK to oscillation parameters is assessed by a combined fit of beam and atmospheric samples. For the atmospheric part, SK atmospheric Monte Carlo (MC) is adapted and scaled to HK statistics. A total of 2224 bins are used, divided in several two-dimensional histograms of $\log p$ and $\cos \vartheta$, where ϑ is the azimuthal angle. The beam sample uses four histograms in reconstructed energy with 87 bins for each of the four event samples, 1 ring e -like and 1 ring μ -like events in ν and $\bar{\nu}$ mode. The event rates at the far detector are estimated with a flux prediction tuned with near detector constraints and smeared to obtain the reconstructed energy spectra. The event distributions are then weighted by the corresponding oscillation probabilities for each point of the oscillation space, using the true neutrino energy.

The oscillation space spans four variables, Δm_{32}^2 , $\sin^2 2\theta_{13}$, $\sin^2 \theta_{23}$, and δ_{CP} , on a grid of respectively $13 \times 13 \times 13 \times 61$ points. The CP phase is varied on the interval $[-\pi, +\pi]$, whereas the other three parameters are centred around the best fit points from T2K [11] and reactor experiments [12, 13]. The number of events on each point of such space is compared to the number of events of a selected point,

which is referred to as the *true* set of oscillation parameters. A χ^2 -test is used to test CP conservation. The sensitivity of HK to exclude the null hypothesis, *i.e.* $\delta_{CP} = 0, \pm\pi$, is quantified by changing the *true* value of δ_{CP} and by computing

$$\sigma = \sqrt{\min_{\delta_{CP}=0,\pm\pi} \chi^2 - \chi^2_{true}}, \quad (5.4)$$

for each point, where χ^2_{true} is evaluated at the *true* point.

The test statistics of this analysis is defined as a “pull approach” χ^2 [14], in the following way

$$\chi^2_{tot} = 2 \sum_n^{\text{obs}} \left[E_n (1 + \sum f_j^n \varepsilon_j) - O_n + O_n \log \left(\frac{E_n (1 + \sum_j f_j^n \varepsilon_j)}{O_n} \right) \right] + \sum_{ij}^{\text{syst}} \varepsilon_i \rho_{ij}^{-1} \varepsilon_j, \quad (5.5)$$

where O_n and E_n are respectively the number of observed and expected events in the n -th bin and ρ is the inverse of the correlation matrix of the systematic errors. The systematic uncertainties are embedded in the f_j^n term, which is the fractional change induced on the n -th bin by a 1σ variation of the j -th systematic; the amount of the shift is quantified by the “pull” ε_j in units of the uncertainty σ_j . For most of the systematic parameters, a linear response is assumed. This means that varying of the j -th systematic by a known amount, $\beta_j \rightarrow \beta_j + \varepsilon_j \sigma_j$, the number of expected events changes as $E_n \rightarrow E_n (1 + \varepsilon_j f_n^j)$. Certain systematic uncertainties do not present a linear behaviour for small values of ε and they are better described by a linear interpolation between four different f_j^n histograms, computed at $\pm 1\sigma$ and $\pm 3\sigma$. For each point of the oscillation parameter space, the χ^2 is profiled with respect to the pulls. This leads to a set of j non-linear equations, which can be solved iteratively if the condition $\sum_j f_j^n \varepsilon_j < 1$ holds.

We adopt 67 systematics for the atmospheric sample from SK atmospheric studies [15]. For the beam part, the T2K (2018) error model is employed [16], initially uncorrelated with the atmospheric systematic set. There are 74 uncertainties for flux and cross-section parameters, from near detector constraints. They are grouped in 50 systematics—25 for the ν mode and 25 for the $\bar{\nu}$ mode—for the main flux components (ν_e , ν_μ , $\bar{\nu}_e$, and $\bar{\nu}_\mu$), and 24 systematics for cross-section parameters. There are also 45 uncertainties for SK detector efficiencies and Final State Interactions, which parameterise the uncertainties on the four final state event selections at the far detector: 1 ring e -like and 1 ring μ -like in both ν and $\bar{\nu}$ modes. Among these, one systematic describes the energy scale uncertainty.

5.4 Systematic studies and conclusions

It is expected that larger systematic errors will result in a worse sensitivity, but certain uncertainties affect the measurement of CP violation more than others. For example, these can be the ν_e and $\bar{\nu}_e$ charged-current cross sections, the transverse flux model, the pion absorption probability, the total energy scale in SK, or the flux alignment. We study the impact of these selected systematics by modifying them one by one with respect to the nominal model and comparing the overall sensitivities

to CP violation in these different scenarios. Doing so, it is possible to determine which systematics have the most important repercussion on the sensitivity, since it is fundamental to understand their effect at all phases of the experiment.

CP violation in the leptonic sector is plausible and it is also a necessary ingredient for leptogenesis. Neutrino oscillation experiments can lead to the discovery of CP violation, and it is foreseen that HK will determine the value of δ_{CP} , a milestone which requires precise measurements and a deep understanding of the systematic errors.

Chapter 6

HNL searches at DUNE

Heavy nearly-sterile neutrinos are a common ingredient in extensions of the Standard Model which aim to explain neutrino masses, like for instance in Type I seesaw models, or one of its variants. If the scale of the new Heavy Neutral Leptons (HNLs) is sufficiently low, observable signatures can arise in a range of current and upcoming experiments, from the LHC to neutrino experiments. In this article, we discuss the phenomenology of sterile neutrinos in the MeV to GeV mass range, focusing on their decays. We embed our discussion in a realistic mass model and consider the resulting implications. We focus in particular on the impact on the signal of the strong polarisation effects in the beam for Majorana and (pseudo-)Dirac states, providing formulae to incorporate these in both production and decay. We study how the Near Detector of the upcoming Deep Underground Neutrino Experiment can constrain HNL states by searching for their decay products inside the detector. We conduct a Monte Carlo background analysis for the most promising signatures, incorporating the detector's particle identification capabilities, and estimate the experimental sensitivity of DUNE to these particles. We also present an estimate of the ν_τ -derived HNL flux at DUNE, currently missing in the literature, which allows us to discuss searches for HNLs at higher masses.

6.1 Introduction

The evidence for three neutrino flavour oscillation is well established [? ?] and can be accounted for only if neutrino mass splittings are non zero [?]. This implies that neutrinos are massive and mix, forcing to consider extensions of the Standard Model (SM) to explain their origin. A simple means of doing so is to introduce the right-handed counterpart of SM neutrinos, which are singlet with respect to all SM gauge symmetries. The Lagrangian includes a Yukawa coupling between these sterile states, the Higgs boson and the leptonic doublet, which generates Dirac mass-terms below the scale of Electroweak Symmetry Breaking (EWSB), and Majorana mass terms for the new singlet states. On diagonalisation of the resulting neutrino mass matrix, the heavy neutrino states, commonly known as nearly-sterile neutrinos or Heavy Neutral Leptons (HNLs) in experimental contexts, remain mainly in

the sterile neutrino direction and have sub-weak interactions suppressed by elements of the extended Pontecorvo-Maki-Nakagawa-Sakata (PMNS) mixing matrix.

These states have been connected to a vast range of phenomenological behaviours and even to cosmological implications (for a recent review on sterile neutrinos, see *e.g.*Ref. [?]). For instance, nearly-sterile neutrinos in the keV region are viable warm Dark Matter candidates (see *e.g.*Ref. [?]), whereas heavier HNLs could play a role in leptogenesis [4? ? ? ? ? ? ? ? ? ?]. So far, some possible hints in favour of heavy neutrinos have emerged in neutrino appearance oscillation experiments, specifically LSND [?] and MiniBooNE [? ? ?] but are disfavoured by disappearance experiments [? ? ?], unless non-standard effects are present [? ? ? ?]. Further hints in the same mass range have been reported for mixing with electron neutrinos in the so-called reactor anomaly [? ? ? ? ?] and in the less statistically significant Gallium one [? ? ?]. Explanations of the MiniBooNE low energy excess invoking GeV-scale HNLs with non-standard interactions [? ? ? ? ?], have also been put forward. In these models, heavy neutral fermions are produced by neutrino up-scattering in the detector and subsequently decaying into photons or electrons, which mimic an electron neutrino interaction. The interpretation of the current experimental results is still largely debated in the scientific community. Searches both for electron-like signatures in MicroBooNE, the SBN programme at Fermilab [?], and in short baseline reactor neutrino experiments, such as DANNS [?], NEOS [?], PROSPECT [?], STEREO [?], NEUTRINO-4 [?], will shed further light on these possibilities.

Apart from these controversial hints, no positive evidence of heavy neutrinos has been found to date in laboratory searches. A thorough review of the current constraints can be found in Refs. [17, 18]. Bounds critically depend on the HNL masses and the flavour with which they mix. Searches for kinks in Curie plots of β -decay spectra [? ? ? ? ?] have placed bounds on the electronic mixing for HNL masses between the keV and MeV scales. For masses from a few MeV to a few hundreds MeV, searches for monochromatic peaks in the lepton spectrum of decaying pions and kaons place important bounds on the muonic and electronic mixing angles [19? ? ? ?]. Neutrinoless double beta decay indirectly constrains Majorana HNLs from the eV to the TeV scale and lepton number violating meson and tau decays can be used to set limits on the mixing angle in narrow ranges of HNLs masses [17]. The tightest constraints come from searches for the direct production and subsequent decays of heavy neutrinos in *beam dump* experiments and at colliders. The strongest limits were set by the PS191 experiment [? ?], a beam dump experiment which ran at CERN in 1984. Its most stringent upper bounds on the novel mixing angles are $|U_{e4}|^2, |U_{\mu 4}|^2 \leq 10^{-8} - 10^{-9}$ for neutrino masses between the pion and the kaon mass. Other bounds of this type can be found in Refs. [20? ? ? ? ?, 21] as well as collider ones, from LHCb [?], ATLAS [?], CMS [? ?], BELLE [?] (see also Ref. [?]).

It is exciting to note that current and upcoming neutrino oscillation experiments will be able to perform beam dump style measurements [? ? ?]. A crucial difference between oscillation detectors and dedicated beam dump searches of the past is that the former tries to maximise its Standard Model

neutrino scattering rate, while the latter goes to lengths to suppress it in order to reduce backgrounds. However, for some of the current and future accelerator neutrino experiments, such as the Short Baseline Neutrino (SBN) program [?], the strong particle reconstruction capabilities of Liquid Argon detectors and distinctive kinematics of neutrino decays have been shown to allow competitive bounds on heavy neutrinos to be made despite naively large backgrounds [?]. Long baseline oscillation experiments, such as the upcoming Deep Underground Neutrino Experiment (DUNE) [?], will see a greatly diluted flux of nearly-sterile neutrinos at their far detectors and consequently poor sensitivity. However, the DUNE Near Detector (DUNE ND), placed 574 m from the target, has a great potential for searches for new physics [?]. Even if the final design of the ND has not been confirmed as yet, the options being considered combine a large active volume, in close proximity to a very intense neutrino beam and cutting-edge event reconstruction capabilities. These will allow DUNE ND to undertake valuable searches for BSM physics in a entirely complementary way to the central oscillation physics programme.

In this article, we present a detailed analysis of the sensitivity of DUNE ND to HNL in beam dump style searches. Differently from previous sensitivity studies [? ?], we ground our discussion in theoretically consistent models, in which sterile neutrinos are associated with neutrino mass generation via a low-scale seesaw mechanism. We note that the range of masses and mixing angles testable at DUNE ND is of interest for the generation of the baryon asymmetry in the context of the ASR mechanism [? ? ? ? ?]. We consider both Majorana and pseudo-Dirac states and calculate their decay and production rates, with careful consideration given to helicity arguments. These formulae are then used to estimate the sensitivity of the experiment, taking into account the beam and detector performance capabilities thanks to simulations of both event and background signals. We stress that DUNE will be able to extend the current limits on new fermionic singlets, including those with masses above 500 MeV, probing models of theoretical significance for the generation of neutrino mass. We show that bounds can be put also on the mixing with tau neutrinos, thanks to the high energy beam.

The article is organised as follows. In Section 6.2 we discuss neutrino mass generation and its consequences for heavy neutrinos in the mass range of interest. In Section 6.3 and Section 6.4, we present the nearly-sterile neutrino decay and production rates accounting for both Majorana/(pseudo-)Dirac states and fully incorporating helicity effects and distributional information about the final-state observables. In Section 6.5, we turn to DUNE ND, describing our assumptions about the experimental apparatus, our neutrino flux modelling, including a $\nu_\tau/\bar{\nu}_\tau$ simulation, the expected signal and the impact of backgrounds. In Section 6.6, we quantify the sensitivity of DUNE ND to decays of heavy neutrino and, in Section 6.7, its ability to constrain the parameter space of low-scale seesaw models. Our concluding remarks are made in Section ??.

6.2 Heavy neutrinos in seesaw models

The lightness of the observed neutrino masses can be explained in a range of different scenarios. New SM-gauge singlet fermions are a feature common to many of them. The most general Lagrangian including a set of right-chiral gauge singlets $\{\mathcal{N}_i\}$ is given by

$$\mathcal{L}_{\text{SM}+\mathcal{N}} = \mathcal{L}_{\text{SM}} + i\bar{\mathcal{N}}_i \partial^\mu \mathcal{N}_i + Y_{\alpha i} \bar{L}_\alpha \tilde{H} \mathcal{N}_i + \frac{1}{2} (M_R)_{ij} \bar{\mathcal{N}}^c_i \mathcal{N}_j + \text{h.c.} , \quad (6.1)$$

with \mathcal{L}_{SM} denoting the SM Lagrangian and the other symbols taking their conventional meaning. Without loss of generality, M_R can be chosen to be diagonal. After electroweak symmetry breaking, a Dirac mass emerges for which we will use the notation $m_D \equiv vY/\sqrt{2}$. This term appears, for instance, in the famous Type I seesaw mechanism [22? ?, 23]. Majorana masses for the light neutrinos arise and are given by

$$m_\nu = -m_D M_R^{-1} m_D^T + \mathcal{O}\left([m_D M_R^{-1}]^2\right) . \quad (6.2)$$

The heavy neutrino masses are approximately given by the diagonal entries of M_R and its corresponding eigenstates, the heavy nearly-sterile neutrinos N_i , have suppressed mixing with active neutrinos and are mainly composed by sterile fields. Neglecting the matrix nature of these expressions for now, if m_D takes values around the electroweak scale, acceptable neutrino masses are produced when M_R has values around the GUT scale, suggestively connecting it to a high-scale breaking of $U(1)_{B-L}$ [?]. Low-scale solutions are also possible by taking the Yukawa couplings to be similar or smaller than the other SM lepton Yukawa couplings, *e.g.*if m_D takes values in the keV range, new nearly-sterile states would exist with masses around a GeV. Although the mass scale for the heavy neutrino can span many orders of magnitude, the resulting mixing is constrained by the contribution given to light neutrino masses

$$|U_{\alpha N}|^2 \lesssim \frac{m_\nu}{m_N} \lesssim 10^{-10} \frac{1 \text{ GeV}}{m_N} , \quad (6.3)$$

where we have taken $m_\nu \lesssim 0.1 \text{ eV}$. These suppressed mixing angles make experimental searches for heavy neutrinos in this range particularly challenging, and beyond the capabilities of most experiments to-date.

In recent years a lot of interest has focused on more complex models with multiple new fermion states, *e.g.*the Inverse Seesaw (ISS) [? ?], extended seesaw [?] and linear seesaw models [? ?]. In these cases the bound in Eq. (6.3) can be avoided because of the cancellation between the contributions to neutrino masses by a different sterile neutrino. For definiteness, we will focus on the ISS model. In this case, a quasi-preserved lepton number guarantees the specific texture of M_R and m_D and its small breaking is natural in the 't Hooft sense [?].

The physical spectrum of heavy neutrinos can be best understood in the Lepton Number Conserving (LNC) limit. We use ISS (a, b) to denote the model with a (b), $a, b \neq 0$, new gauge singlets of lepton

number $+1$ (-1). Following Eq. (6.1) and Eq. (6.2), the most general mass matrices are then given by

$$m_D = \begin{pmatrix} m, 0 \end{pmatrix} \quad \text{and} \quad M_R = \begin{pmatrix} 0 & M^T \\ M & 0 \end{pmatrix},$$

where we introduce the $3 \times a$ complex matrix m and the $b \times a$ complex matrix M . The spectrum of physical states in the LNC limit for ISS (a, b) is given by

$$\min\{3 + b, a\} \text{ Dirac pairs} \quad \text{and} \quad |3 + b - a| \text{ massless Weyl states.}$$

The masses of the Dirac pairs are the non-zero singular values of the rectangular $a \times (3 + b)$ matrix (m^T, M^T) . Note that for $a \neq b$, in addition to a set of Dirac pairs of arbitrary masses, extra massless sterile states degenerate with the light neutrinos are present. Mixing involving these degenerate states is not defined in the LNC limit, as any unitary map in the degenerate subspace is permissible. On the contrary, the introduction of a small Lepton Number Violating (LNV) parameter perturbs the LNC spectrum as well as the mixing. In general there are only two possible origins for a low-scale heavy neutrino:

- A massless Weyl fermion in the LNC limit which is given non-zero mass proportional to the perturbation. As the mixing between massless states is not defined in the LNC limit, the perturbation controls the induced mixing between the nearly-sterile state and the active ones. We will refer to this state as a Majorana neutrino.
- A massive Dirac pair at the low scale in the LNC limit, becoming a pseudo-Dirac pair after the perturbation, which regulates the mass splitting of the pair. In the LNC limit, the mixing angles between Dirac pair and light neutrinos can be arbitrarily large, and this property remains after the perturbation.

The first case only arises in models with an imbalanced number of new fields, *i.e.*ISS (a, b) such that $a \neq b$, while the second option can occur in any ISS model.

In this paper, we are interested in heavy states with masses in the MeV–GeV range.¹ Our discussion above suggests that both Majorana states and (pseudo-)Dirac states should be considered, covering all possible phenomenological aspects. In what follows, we will compute the production and decay rates for Majorana states and Dirac states and study their discovery potential at DUNE ND. We disregard lepton number violating effects and therefore the distinction between pseudo-Dirac and Dirac states will not be relevant.

Feynman rules for Majorana states derived from Eq. (6.1) can be found in [17], or constructed using the techniques of Ref. [?]. For an explicit comparison between Dirac versus Majorana Feynman rules for heavy neutrinos, see Ref. [?].

¹This is motivated by the kinematic limits on production from meson decays discussed in more detail in Section 6.4.

6.3 Heavy neutrino decay

In this section we compute the heavy neutrino decay rates and polarised distributions necessary for the simulation of beam dump searches. We compute rates for both Majorana and (pseudo-)Dirac states, allowing us to consistently explore the parameter space of low-scale seesaw models.

This analysis can be simplified by noting the following equivalences. A Majorana neutrino N decaying via a charged current process has the same differential decay rate as the Dirac neutrino N_D with the appropriate lepton number,

$$d\Gamma(N \rightarrow \ell_\alpha^- X^+) = d\Gamma(N_D \rightarrow \ell_\alpha^- X^+) \quad \text{and} \quad d\Gamma(N \rightarrow \ell_\alpha^+ X^-) = d\Gamma(\bar{N}_D \rightarrow \ell_\alpha^+ X^-),$$

where we assume identical mass and mixing angles for both Dirac and Majorana neutrinos. This equivalence can be seen directly from the Feynman rules for Dirac and Majorana fermions [?] (see also Ref. [?]), but also explicitly in our formulae below. In a neutral current (NC) decay, however, the two contractions of the NC operator lead to another contribution,

$$d\Gamma(N \rightarrow \nu X') = d\Gamma(N_D \rightarrow \nu X') + d\Gamma(\bar{N}_D \rightarrow \bar{\nu} X').$$

These relations hold at the differential level if the kinematic variables are reinterpreted in the obvious way. In this sense, we can view the Majorana process as the sum of Dirac particle and antiparticle decays.² Considering the total decay rates only, we find that the Majorana decay is larger by a factor of 2 compared to the Dirac case,

$$\Gamma(N \rightarrow \nu X') = 2\Gamma(N_D \rightarrow \nu X').$$

Note that this is true only for the total decay rates with massless final-state neutrinos.

It is instructive to reconsider this result in the light of the *practical Dirac–Majorana confusion theorem* [? ?]. In Ref. [?], the decomposition into particle and antiparticle processes was performed for Majorana neutrino–electron scattering via neutral current, leading to a factor of two enhancement in the total rate. However, this enhancement was shown to be absent in practice due to the polarisation of the incoming neutrino, which suppresses the $\Delta L = 2$ contributions by factors of the neutrino mass. In the present case of nearly-sterile decay, where mass effects are large and essential to the calculation, there is no analogous effect: Dirac and Majorana neutrinos will have distinct total decay rates regardless of their polarisation. Therefore, the total decay rates of heavy neutrinos into observable final states could in principle allow us to determine the Majorana/Dirac nature of the initial state. This is not a trivial effect: a pure Majorana state decays with equal probability into $e^- \pi^+$ as $e^+ \pi^-$, one of its dominant and most experimentally distinctive branching decay modes, while a Dirac heavy neutrino

²In a general amplitude with Majorana states, there would also be an interference contribution between these two sub-processes. However, in all cases of interest, interference diagrams are proportional to the final-state light neutrino mass, which we take to be zero.

Channel	Threshold	Channel	Threshold	Channel	Threshold
$\nu\nu\nu$	10^{-9} MeV	$e^\mp K^\pm$	494 MeV	$\nu\eta'$	958 MeV
$\nu e^+ e^-$	1.02 MeV	$\nu\eta$	548 MeV	$\mu^\mp K^{*\pm}$	997 MeV
$\nu e^\pm \mu^\mp$	105 MeV	$\mu^\mp K^\pm$	559 MeV	$\nu\phi$	1019 MeV
$\nu\pi^0$	135 MeV	$\nu\rho^0$	776 MeV	$\nu e^\pm \tau^\mp$	1776 MeV
$e^\mp\pi^\pm$	140 MeV	$e^\mp\rho^\pm$	776 MeV	$e^\mp D^\pm$	1870 MeV
$\nu\mu^+\mu^-$	210 MeV	$\nu\omega$	783 MeV	$\nu\mu^\pm\tau^\mp$	1880 MeV
$\mu^\mp\pi^\pm$	245 MeV	$\mu^\mp\rho^\pm$	882 MeV	$\tau^\mp\pi^\pm$	1870 MeV
		$e^\mp K^{*\pm}$	892 MeV		

Tab. 6.1: All the available channels for a HNL with a mass below the D_s^\pm mass are listed above, sorted by threshold mass. The active neutrino is considered massless, when compared to the masses of the other particles.

Fig. 6.1: The branching ratios for HNL decays, integrated over the angular variables, are shown above as functions of the mass. They are grouped in CC-mediated decays (left) and NC-mediated decays (right), in the range from 0.01 MeV up to the maximum mass limit for neutrino production, near 2 GeV. A scenario in which $|U_{eN}|^2 = |U_{\mu N}|^2 = |U_{\tau N}|^2$ is chosen here for illustrative purposes. The branching ratios of Majorana neutrinos and Dirac neutrinos are mathematically identical and therefore no distinction is stressed. The decay into three light neutrinos is fundamental for a correct computation of the branching ratios, even though fully invisible from an experimental point of view.

will only decay into $e^-\pi^+$. Assuming charge-identification is possible in the detector, distinguishing between the two total decay rates should be possible with modest statistics. In a charge-blind search or for an NC channel, the total decay rate of Majorana neutrinos would appear to be twice as large as that of Dirac neutrinos. However, being the mixing usually an unknown quantity, the difference between Majorana and Dirac nature cannot be deduced as easily.

There is also a more subtle impact of the nature of the decaying neutrino. Even though the total decay rate is not affected by the helicity of the initial neutrino, the helicity does affect the distributions of final state particles, which will in turn influence the observability of the signatures of neutrino decay. It is important that these polarisation effects are correctly implemented when studying the distributions of final state observables and subsequently when developing an analysis to tackle backgrounds.

In the remainder of this section, we present results for the polarised heavy neutrino decay rates and distributions for Majorana and (pseudo-)Dirac neutrinos. The decay modes considered are listed in Tab. 6.1 and the respective branching ratios as functions of the neutrino mass are shown in Fig. 6.1. The differential widths have been computed using the massive spinor helicity formalism (see *e.g.* Refs. [? ?]), and checked numerically using FeynCalc [? ?].

6.3.1 Polarised Majorana neutrino decay

Although spin-averaged Majorana neutrino decay rates are well known in the literature [17? ?] (see also Ref. [?]), to the best of our knowledge the polarised rates are not. These are necessary to correctly describe the distributions of observables in a beam dump experiment, and in this section we present formulae for these differential decay rates.

Note that we stay agnostic as to the final nature and flavours of outgoing neutrinos, and in all cases sum over any possible outgoing states to define a semi-inclusive decay rate into the visible particle(s) X' , *i.e.*

$$\Gamma(N \rightarrow \nu X') \equiv \sum_{i=1}^3 \Gamma(N \rightarrow \nu_i X') .$$

The alternative, chosen by many other authors, is to treat light neutrinos as Dirac particles, and construct the full decay width using arguments of CP invariance, in practice amounting to adding some judicious factors of two [17?]. Following this approach, our summed decay rate for $N \rightarrow \nu X'$ can be seen as

$$\Gamma(N \rightarrow \nu X') \equiv \sum_{\alpha=e}^{\tau} [\Gamma(N \rightarrow \nu_\alpha X') + \Gamma(N \rightarrow \bar{\nu}_\alpha X')] .$$

The two approaches are identical mathematical procedures and can both be used to compute the differential decay rates; however, we avoid the latter as the light neutrinos in most seesaw models are Majorana fermions, and making a distinction between ν_α and $\bar{\nu}_\alpha$ is physically misleading.³ We also find that the distribution of events, the role of helicity and the heavy neutrino nature are obscured by this approach. In contrast, by summing over all outgoing states, our formulae are insensitive to the Majorana/Dirac nature of the light neutrinos, and are the physically relevant rates necessary for comparison with beam dump experiments, as outgoing neutrinos are not reconstructed.

Pseudoscalar mesons

The semi-leptonic meson decays are some of the most important channels identified in previous studies [17?] (see also Ref. [?]) thanks to their large branching ratios and distinctive final state particles. Both charged and neutral pseudo-scalar mesons are viable final state particles, namely P^\pm and P^0 , and the decay widths are given in the Centre of Mass (CM) frame by

$$\frac{d\Gamma_\pm}{d\Omega_{\ell_\alpha}}(N \rightarrow \ell_\alpha^- P^+) = |U_{\alpha N}|^2 |V_{q\bar{q}}|^2 \frac{G_F^2 f_P^2 m_N^3}{16\pi} I_1^\pm(\xi_\alpha^2, \xi_P^2; \theta_\alpha) , \quad (6.4)$$

$$\frac{d\Gamma_\pm}{d\Omega_{\ell_\alpha}}(N \rightarrow \ell_\alpha^+ P^-) = |U_{\alpha N}|^2 |V_{q\bar{q}}|^2 \frac{G_F^2 f_P^2 m_N^3}{16\pi} I_1^\mp(\xi_\alpha^2, \xi_P^2; \theta_\alpha) , \quad (6.5)$$

$$\frac{d\Gamma_\pm}{d\Omega_P}(N \rightarrow \nu P^0) = \left(\sum_{\alpha=e}^{\tau} |U_{\alpha N}|^2 \right) \frac{G_F^2 f_P^2 m_N^3}{16\pi} \frac{I_1(0, \xi_P^2)}{4\pi} , \quad (6.6)$$

where Γ_h is the decay rate for neutrinos of helicity h , $V_{q\bar{q}}$ is the appropriate CKM matrix element for the considered meson, f_P is its decay constant and $\xi_i = m_i/m_N$ denotes the mass of the final state particle i as a fraction of the initial state mass. The solid angle elements Ω_{ℓ_α} and Ω_P refer respectively to the charged lepton and pseudo-scalar meson angle with respect to the neutrino direction. The kinematic function $I_1(x, y)$ [17] and its angular generalisation accounting for helicity, $I_1^\pm(x, y; \theta)$, are defined in Appendix 6.8. After integrating over the angular variables, we find that both the pseudo-scalar meson

³The approach could be seen as a short-hand for decay rates into polarised massless neutrinos, but as we are particularly concerned with polarisation effects in the beam this only adds a further complication.

decay rates do not depend on helicity, as expected,

$$\Gamma_{\pm}(N \rightarrow \ell_{\alpha}^{-} P^{+}) = \Gamma_{\pm}(N \rightarrow \ell_{\alpha}^{+} P^{-}) = |V_{q\bar{q}}|^2 |U_{\alpha N}|^2 \frac{G_F^2 f_P^2 m_N^3}{16\pi} I_1(\xi_{\alpha}^2, \xi_P^2), \quad (6.7)$$

$$\Gamma_{\pm}(N \rightarrow \nu P^0) = \left(\sum_{\alpha=e}^{\tau} |U_{\alpha N}|^2 \right) \frac{G_F^2 f_P^2 m_N^3}{16\pi} I_1(0, \xi_P^2). \quad (6.8)$$

These rates agree with those presented in Refs. [? ?] (correcting a factor of two discrepancy in the νP^0 rate of Refs. [17?]).

The decay into a neutral meson, in Eq. (6.6), is isotropic in the rest frame, while the charged-pion modes, Eqs. (6.4) and (6.5), inherit their angular dependence from $I^{\pm}(x, y; \theta_{\alpha})$, on the lepton angle to the beam line in the heavy neutrino rest frame θ_{α} . The isotropy of the neutral current decay $N \rightarrow \nu P^0$ is a manifestation of the Majorana nature of the particle, in agreement with the discussion of Ref. [?]. It is worth noting that, if final states are not charge-identified, a similar isotropy is obtained for the total rate of charged semi-leptonic decays,

$$\begin{aligned} \frac{d\Gamma_{\pm}}{d\Omega_{\ell_{\alpha}}}(N \rightarrow \ell_{\alpha} P) &\equiv \frac{d\Gamma_{\pm}}{d\Omega_{\ell_{\alpha}}}(N \rightarrow \ell_{\alpha}^{+} P^{-}) + \frac{d\Gamma_{\pm}}{d\Omega_{\ell_{\alpha}}}(N \rightarrow \ell_{\alpha}^{-} P^{+}) \\ &= |U_{\alpha N}|^2 |V_{q\bar{q}}|^2 \frac{G_F^2 f_P^2 m_N^3}{16\pi} \frac{I_1(\xi_{\alpha}^2, \xi_P^2)}{2\pi}. \end{aligned} \quad (6.9)$$

The formulae above apply for all pseudo-scalar mesons which are kinematically allowed. For instance, below the K^0 mass, the heavy neutrino can decay only into pions, but above η and η' can be allowed in the final state.

Vector mesons

Although only for higher masses, HNL can also decay into vector mesons V , both via charged current, $N \rightarrow \ell^{\mp} V^{\pm}$, and neutral current, $N \rightarrow \nu V^0$. We find the following polarised differential distributions in the heavy neutrino rest frame,

$$\frac{d\Gamma_{\pm}}{d\Omega_{\ell_{\alpha}}}(N \rightarrow \ell_{\alpha}^{-} V^{+}) = |U_{\alpha N}|^2 |V_{q\bar{q}}|^2 \frac{G_F^2 f_V^2 m_N^3}{16\pi} I_2^{\pm}(\xi_{\alpha}^2, \xi_V^2; \theta_{\alpha}), \quad (6.10)$$

$$\frac{d\Gamma_{\pm}}{d\Omega_{\ell_{\alpha}}}(N \rightarrow \ell_{\alpha}^{+} V^{-}) = |U_{\alpha N}|^2 |V_{q\bar{q}}|^2 \frac{G_F^2 f_V^2 m_N^3}{16\pi} I_2^{\mp}(\xi_{\alpha}^2, \xi_V^2; \theta_{\alpha}), \quad (6.11)$$

$$\frac{d\Gamma_{\pm}}{d\Omega_V}(N \rightarrow \nu V^0) = \left(\sum_{\alpha=e}^{\tau} |U_{\alpha N}|^2 \right) \frac{G_F^2 f_V^2 \kappa_V^2 m_N^3}{16\pi} \frac{I_2(0, \xi_V^2)}{4\pi}, \quad (6.12)$$

where $I_2(x, y)$ and $I_2^{\pm}(x, y; \theta)$ are defined in Appendix 6.8. We find the total decay widths given by

$$\Gamma(N \rightarrow \ell_{\alpha}^{-} V^{+}) = \Gamma(N \rightarrow \ell_{\alpha}^{+} V^{-}) = |U_{\alpha N}|^2 |V_{q\bar{q}}|^2 \frac{G_F^2 f_V^2 m_N^3}{16\pi} I_2(\xi_{\alpha}^2, \xi_V^2), \quad (6.13)$$

$$\Gamma(N \rightarrow \nu V^0) = \left(\sum_{\alpha=e}^{\tau} |U_{\alpha N}|^2 \right) \frac{G_F^2 f_V^2 \kappa_V^2 m_N^3}{16\pi} I_2(0, \xi_V^2), \quad (6.14)$$

where the constants κ_V are combinations of the Weinberg angle, depending on the flavour structure of V^0 (see below). Our charged pseudo-vector decay rates agrees with Refs. [17? ? ?] while our neutral pseudo-scalar calculation agrees with the corrected version presented in Ref. [?].

As with the pseudo-scalar meson decay rates, the Majorana nature leads to an isotropic decay into a neutral vector meson. An analogous effect holds for the charged vector meson decay if we assume that the charges of final state particles are not distinguished. In this case, we find the physically relevant decay distribution in the particle rest frame to be given by

$$\begin{aligned} \frac{d\Gamma_{\pm}}{d\Omega_{\ell_{\alpha}}}(N \rightarrow \ell_{\alpha} V) &\equiv \frac{d\Gamma_{\pm}}{d\Omega_{\ell_{\alpha}}}(N \rightarrow \ell_{\alpha}^- V^+) + \frac{d\Gamma_{\pm}}{d\Omega_{\ell_{\alpha}}}(N \rightarrow \ell_{\alpha}^+ V^-) , \\ &= |U_{\alpha N}|^2 \frac{G_F^2 f_V^2}{16\pi} |V_{q\bar{q}}|^2 m_N^3 \frac{I_2(\xi_{\alpha}^2, \xi_V^2)}{2\pi} . \end{aligned} \quad (6.15)$$

There are no vector mesons lighter than the K^0 , and these decays become relevant only for higher masses for which decays into ρ^{\pm} and $K^{*\pm}$, and for the neutral mode into ρ^0 , ω , and ϕ would be relevant. For these neutral particles, the κ_V factors read

$$\kappa_{\rho} = 1 - \sin^2 \theta_W , \quad \kappa_{\omega} = \frac{4}{3} \sin^2 \theta_W , \quad \kappa_{\phi} = \frac{4}{3} \sin^2 \theta_W - 1 .$$

Charged lepton pairs

We assign the momenta to the particles in the three-body decay as follows

$$N(k_1) \rightarrow \nu(k_2) \ell_{\alpha}^-(k_3) \ell_{\beta}^+(k_4) ,$$

and denote $k_i^2 = m_i^2$. The five-dimensional phase space of the final-state particles can be parameterised using two scaled invariant masses,

$$s_1 = \frac{(k_2 + k_3)^2}{m_N^2} \quad \text{and} \quad s_2 = \frac{(k_2 + k_4)^2}{m_N^2} ,$$

as well as three lab-frame angular variables, (θ_3, ϕ_3) , giving the direction of ℓ_{α}^- and φ_{43} denoting the relative azimuthal angle between ℓ_{α}^- and ℓ_{β}^+ . Although $\cos \theta_4$ is not an independent element of our parametrisation, it is a physically relevant quantity and we use it to simplify the presentation of the distributions below. It can be easily related to the fundamental variables $s_1, s_2, \theta_3, \varphi_3, \varphi_{43}$. The differential decay rate is expressed as

$$d\Gamma_{\pm} = \frac{G_F^2 m_N^5}{16\pi^3} (|A_0|^2 \pm |A_1|^2) ds_1 ds_2 \frac{d^2\Omega_3}{4\pi} \frac{d\varphi_{43}}{2\pi} , \quad (6.16)$$

where Ω_3 assumes the conventional meaning and with

$$\begin{aligned} |A_0|^2 &\equiv C_1(s_2 - \xi_3^2)(1 + \xi_4^2 - s_2) + C_2(s_1 - \xi_4^2)(1 + \xi_3^2 - s_1) \\ &\quad + 2C_3 \xi_3 \xi_4 (s_1 + s_2 - \xi_3^2 - \xi_4^2) , \end{aligned} \quad (6.17)$$

$$\begin{aligned} |A_1|^2 &\equiv [C_4(s_2 - \xi_3^2) - 2C_6 \xi_3 \xi_4] \lambda^{\frac{1}{2}}(1, s_2, \xi_4^2) \cos \theta_4 \\ &\quad + [C_5(s_1 - \xi_4^2) - 2C_6 \xi_3 \xi_4] \lambda^{\frac{1}{2}}(1, s_1, \xi_3^2) \cos \theta_3 . \end{aligned} \quad (6.18)$$

The coefficients $\{C_i\}$ are polynomials in chiral couplings and extended PMNS matrix elements, and are given for the decays of interest in Appendix 6.9. On integration over the angular coordinates, however,

only the $|A_0|^2$ terms remain and we recover the standard expression for the total decay rates through the identities given in Eqs. (6.44), (6.45) and (6.46). The general expression for the total decay rate is again helicity independent and can be written as

$$\Gamma_{\pm} = \frac{G_F^2 m_N^5}{192\pi^3} [C_1 I_1(0, \xi_3^2, \xi_4^2) + C_2 I_1(0, \xi_4^2, \xi_3^2) + C_3 I_2(0, \xi_3^2, \xi_4^2)] . \quad (6.19)$$

The functions $I_1(x, y, z)$ and $I_2(x, y, z)$ are given in Appendix 6.8. Using the expressions for $\{C_i\}$ in Appendix 6.9, we find that the total decay rates are given to first order in the heavy-active mixing parameters $U_{\alpha N}$ by

$$\Gamma_{\pm}(N \rightarrow \nu \ell_{\alpha}^- \ell_{\beta}^+) = \frac{G_F^2 m_N^5}{192\pi^3} [|U_{\alpha N}|^2 I_1(0, \xi_{\alpha}^2, \xi_{\beta}^2) + |U_{\beta N}|^2 I_1(0, \xi_{\beta}^2, \xi_{\alpha}^2)] , \quad (6.20)$$

$$\begin{aligned} \Gamma_{\pm}(N \rightarrow \nu \ell_{\alpha}^- \ell_{\alpha}^+) = & \frac{G_F^2 m_N^5}{96\pi^3} \sum_{\gamma=e}^{\tau} |U_{\gamma N}|^2 \left\{ (g_L g_R + \delta_{\gamma\alpha} g_R) I_2(0, \xi_{\alpha}^2, \xi_{\alpha}^2) \right. \\ & \left. + [g_L^2 + g_R^2 + \delta_{\gamma\alpha}(1 + 2g_L)] I_1(0, \xi_{\alpha}^2, \xi_{\alpha}^2) \right\} . \end{aligned} \quad (6.21)$$

where $\alpha \neq \beta$, $g_L = -1/2 + \sin^2 \theta_W$ and $g_R = \sin^2 \theta_W$. Our total decay rates agree with those in Refs. [17? ? ?] and correct a typographical mistake in the rates presented in Ref. [?].

All possible combinations of charged leptons except $\nu \tau^- \tau^+$ are allowed for masses below m_{D_s} . However, because of the limited phase space, the decays into $\nu \tau^{\mp} e^{\pm}$ and $\nu \tau^{\mp} \mu^{\pm}$ can be neglected.

Other decays

There are some other decay rates relevant to this study but not as viable observable channels. First, the total decay width of the process $N \rightarrow \nu \bar{\nu} \nu$, mediated by the Z boson, reads

$$\Gamma(N \rightarrow \nu \bar{\nu} \nu) = \left(\sum_{\gamma=e}^{\tau} |U_{\gamma 4}|^2 \right) \frac{G_F^2 m_N^5}{96\pi^3} . \quad (6.22)$$

Although this decay mode is experimentally invisible, it is the dominant channel up to the pion mass, when two-body semi-leptonic decays open up, and plays a significant role in defining the branching ratios of the observable channels. Our expression agrees with Refs. [17? ? ?]. Secondly, there are other decay modes with small branching ratios and/or complicated final states which we do not study further. These include the one-loop decay into a photon which has received some interest as an observable signature in non-minimal models [? ? ?] where it may be enhanced. In the mass models considered in this work, it has a branching ratio of below 10^{-3} and will not be considered. We also neglect the multi-pion decay modes discussed in Ref. [?], which are estimated to have at most a percent level branching ratio and a challenging hadronic final state for reconstruction.

6.3.2 Polarised (pseudo-)Dirac neutrino decay

In this section we compute the decay rates for pseudo-Dirac pairs. It is unlikely that any effect driven by the LNV parameter will be relevant for the discovery potential of DUNE ND and the signatures of

these particles will be dominated by the leading order LNC effects. Accordingly, we take the strict Dirac limit in our calculations, rather than treating the states as pseudo-Dirac pairs.

Dirac (anti)neutrino decays

The decay rates for a Dirac heavy (anti)neutrino are similar in form to those presented for the Majorana neutrino. The key differences are lepton number conservation, which acts to forbid certain channels, and differences in the angular distributions of the neutral current decays. For charged current-mediated processes, the distributions for Dirac neutrinos and antineutrinos are mathematically identical to the distributions for Majorana neutrinos. The two-body semi-leptonic decays are the same of Eqs. (6.4) and (6.10),

$$\frac{d\Gamma_{\pm}}{d\Omega_{\ell_{\alpha}}} (N_D \rightarrow \ell_{\alpha}^- P^+) = \frac{d\Gamma_{\mp}}{d\Omega_{\ell_{\alpha}}} (\bar{N}_D \rightarrow \ell_{\alpha}^+ P^-) = \frac{d\Gamma_{\pm}}{d\Omega_{\ell_{\alpha}}} (N \rightarrow \ell_{\alpha}^- P^+) , \quad (6.23)$$

$$\frac{d\Gamma_{\pm}}{d\Omega_{\ell_{\alpha}}} (N_D \rightarrow \ell_{\alpha}^- V^+) = \frac{d\Gamma_{\mp}}{d\Omega_{\ell_{\alpha}}} (\bar{N}_D \rightarrow \ell_{\alpha}^+ V^-) = \frac{d\Gamma_{\pm}}{d\Omega_{\ell_{\alpha}}} (N \rightarrow \ell_{\alpha}^- V^+) . \quad (6.24)$$

The situation for NC processes is different with respect to Majorana neutrinos. The distribution of the final state particles is not isotropic anymore and it depends on the helicity state of the initial neutrino, in the way shown by the following differential rates

$$\frac{d\Gamma_{\pm}}{d\Omega_P} (N_D \rightarrow \nu P^0) = \frac{d\Gamma_{\mp}}{d\Omega_P} (\bar{N}_D \rightarrow \bar{\nu} P^0) = \left(\sum_{\alpha=e}^{\tau} |U_{\alpha N}|^2 \right) \frac{G_F^2 f_{P^0}^2 m_N^3}{32\pi} I_1^{\pm}(0, \xi_P^2; \theta_P) , \quad (6.25)$$

$$\frac{d\Gamma_{\pm}}{d\Omega_V} (N_D \rightarrow \nu V^0) = \frac{d\Gamma_{\mp}}{d\Omega_V} (\bar{N}_D \rightarrow \bar{\nu} V^0) = \left(\sum_{\alpha=e}^{\tau} |U_{\alpha N}|^2 \right) \frac{G_F^2 f_V^2 \kappa_V^2 m_N^3}{32\pi} I_2^{\mp}(0, \xi_V^2; \theta_V) . \quad (6.26)$$

For the three-body leptonic decays, the distribution is expressed in Eq. (6.16) with the relevant coefficients from Appendix 6.9. The total decay rates are found to be

$$\Gamma_{\pm}(N_D \rightarrow \nu \ell_{\alpha}^- \ell_{\beta}^+) = |U_{\alpha N}|^2 \frac{G_F^2 m_N^5}{192\pi^3} I_1(0, \xi_{\alpha}^2, \xi_{\beta}^2) , \quad (6.27)$$

$$\Gamma_{\pm}(\bar{N}_D \rightarrow \bar{\nu} \ell_{\alpha}^- \ell_{\beta}^+) = |U_{\beta N}|^2 \frac{G_F^2 m_N^5}{192\pi^3} I_1(0, \xi_{\beta}^2, \xi_{\alpha}^2) , \quad (6.28)$$

$$\begin{aligned} \Gamma_{\pm}(N_D \rightarrow \nu \ell_{\alpha}^- \ell_{\alpha}^+) &= \frac{G_F^2 m_N^5}{192\pi^3} \sum_{\gamma=e}^{\tau} |U_{\gamma N}|^2 \left\{ (g_L g_R + \delta_{\gamma\alpha} g_R) I_2(0, \xi_{\alpha}^2, \xi_{\alpha}^2) \right. \\ &\quad \left. + [g_L^2 + g_R^2 + \delta_{\gamma\alpha}(1 + 2g_L)] I_1(0, \xi_{\alpha}^2, \xi_{\alpha}^2) \right\} , \end{aligned} \quad (6.29)$$

$$\Gamma_{\pm}(\bar{N}_D \rightarrow \bar{\nu} \ell_{\alpha}^- \ell_{\alpha}^+) = \Gamma_{\mp}(N_D \rightarrow \nu \ell_{\alpha}^- \ell_{\alpha}^+) , \quad (6.30)$$

where $\alpha \neq \beta$, $g_L = -1/2 + \sin^2 \theta_W$ and $g_R = \sin^2 \theta_W$. Our total decay rates agree with those in Refs. [17? ? ?].

All decay rates not listed above are forbidden for a Dirac (anti)particle as the combination of production and decay would amount to a LNV process. For the available modes, all NC modes are smaller by a factor of two for a Dirac (anti)neutrino compared to the equivalent Majorana process; however, the major difference we see between the Dirac (anti)neutrino and Majorana distributions is

that these NC channels are dependent on the angular variables. These differences in the distributions of the final state particles could be in principle exploited to identify the fermionic nature of the decaying HNL [?].

6.4 Heavy neutrino production

Heavy neutrinos can be produced in a beam dump experiment via the same processes that generate light neutrinos. A proton beam hitting a fixed target typically yields a large number of pions and kaons, and also heavier mesons, the amount of which depends on the energy of the protons and the target choice. A set of magnetic horns is responsible for the focusing of charged pions into a decay pipe; the other short-lived particles are usually unaffected by the deflection. All these secondary particles decay leptonically or semi-leptonically via weak interactions thus creating a neutrino beam. In the standard case of light neutrinos, pions and kaons principally decay into ν_μ because two-body electronic modes are disfavoured by helicity suppression. Muons decay in turn into equal numbers of ν_e and $\bar{\nu}_\mu$. Other production sources of ν_e are the three-body decays of K^0 and K^+ . Above the neutral kaon mass, the first sizeable source of neutrino is given by the D_s meson, for which helicity suppression again favours the production of heavy charged-leptons, and so τ leptons and ν_τ are more likely to be emitted than the other flavours. Each of the subsequent τ^+ decays produces a $\bar{\nu}_\tau$. We consider only the four most probable decay modes of the τ lepton, as they provide a sufficient description of their contribution to the overall flux.⁴

If kinematically allowed, heavy neutrino states can be sourced from these decays of mesons and charged leptons. We show in Tab. 6.2 all the neutrino production channels considered in this analysis, reporting the heaviest neutrino mass m_N that is accessible by kinematics. The neutrino mass range we consider goes from a few MeV up to the D_s meson mass. To estimate the flux of heavy neutrinos produced, we start from the flux of light neutrinos, scaling it by an energy-independent kinematic factor. Given a certain SM neutrino production process, $Q \rightarrow \nu_\alpha Q'$, we use as scale factor the ratio between the decay width of the same process producing massive neutrinos, $Q \rightarrow NQ'$, and the rate of the SM decay with light neutrinos. The full flux of nearly-sterile neutrinos with a given helicity is therefore a linear combination of the different neutrino flux components, $\phi_{Q \rightarrow \nu_\alpha}$, summing over all existing parents and all allowed flavours:

$$\frac{d\phi_N^\pm}{dE}(E_N) \approx \sum_{Q,\alpha} \mathcal{K}_\pm^{Q,\alpha}(m_N) \frac{d\phi_{Q \rightarrow \nu_\alpha}}{dE}(E_N - m_N), \quad (6.31)$$

where

$$\mathcal{K}_\pm^{Q,\alpha}(m_N) \equiv \frac{\Gamma_\pm(Q \rightarrow NQ')}{\Gamma(Q \rightarrow \nu_\alpha Q')}.$$

The ratio \mathcal{K} is proportional to the mixing parameter $|U_{\alpha N}|^2$ and contains only kinematic functions of the involved masses. These are responsible for correcting phase space and helicity terms.

⁴The decay $\tau^+ \rightarrow \bar{\nu}_\tau \pi^+ \pi^0$ is studied only at the level of phase space sampling in this work.

	Channel	BR (%)	m_N (MeV)		Channel	BR (%)	m_N /MeV
$\pi^+ \rightarrow$	$\mu^+ \nu_\mu$	99.98	33.91	$D_s^+ \rightarrow$	$\tau^+ \nu_\tau$	5.48	191.42
	$e^+ \nu_e$	0.01	139.06		$\mu^+ \nu_\mu$	0.55	1862.63
$K^+ \rightarrow$	$\mu^+ \nu_\mu$	63.56	387.81		$e^+ \nu_e$	0.008	1967.78
	$\pi^0 e^+ \nu_e$	5.07	358.19		$\tau^+ \rightarrow$	25.49	1502.31
	$\pi^0 \mu^+ \nu_\mu$	3.35	253.04		$\bar{\nu}_\tau e^+ \nu_e$	17.82	1776.35
	$e^+ \nu_e$	0.16	493.17		$\bar{\nu}_\tau \mu^+ \nu_\mu$	17.39	1671.20
$K_L^0 \rightarrow$	$\pi^\pm e^\mp \nu_e$	40.55	357.12		$\pi^+ \bar{\nu}_\tau$	10.82	1637.29
	$\pi^\pm \mu^\mp \nu_\mu$	27.04	252.38				
$\mu^+ \rightarrow$	$\bar{\nu}_\mu e^+ \nu_e$	100.00	105.14				

Tab. 6.2: Production channels at beam dump facilities yielding neutrinos, with the respective branching ratios (taken from Ref. [?]). The last column shows the maximum neutrino mass allowed if a massive state is produced. On the left, all the decays yielding ν_e , ν_μ , and $\bar{\nu}_\mu$ up to the K^0 mass are shown. On the right, the neutrino sources which depends on the D_s^+ decay chain are shown; only the first four decays of the τ lepton are considered in this work.

The helicity state plays a fundamental role in the production rate, in contrast with the case of neutrino decays, since there is no arbitrariness in the polarisation direction this time: it is defined by the neutrino momentum in the rest frame of the parent particle. We employ the massive spinor helicity formalism to compute the production decay rates for both Majorana and Dirac neutrinos, and these are used to build the scale factors for each neutrino helicity. Even though lepton number is preserved differently in the two cases and different Feynman rules hold, all the production channels of interest in this work are mediated by charge currents and therefore the rates are mathematically identical for Majorana and Dirac neutrinos. If the neutrino is Dirac, the production decay width for an antineutrino with given helicity is the same as the one of the neutrino, but with opposite helicity. The phenomenology of the scale factors is different for two-body decays and three-body decays and therefore we group them, respectively, in Section 6.4.1 and Section 6.4.2.

6.4.1 Two-body decays

A massless neutrino (antineutrino) has its chiral and helicity states degenerate, and so it is always produced with a negative (positive) helicity. It follows that the component of the light neutrino beam produced in two-body decays of pseudo-scalar mesons is polarised. The initial spin, which is zero, must be preserved in the decay, and since the helicity of the neutrino in the rest frame is fixed, the accompanying lepton is produced with a “wrong” helicity. This is permitted by the non-zero mass of the charged lepton and therefore final states with light flavour leptons undergo helicity suppression. As soon as the neutrino mass deviates from zero, the correspondence between chirality and helicity is lost and the neutrino can be produced with both polarisations. The main consequence is that the production of heavy neutrinos from light flavour mixings (electron) appears to be enhanced with respect to heavy

Fig. 6.2: The scale factors separated by helicity components are shown. In two-body decays (left), the $h = -1$ components (dashed) for all channels do not depend on the mass. The enhancement is driven by the $h = +1$ components (dotted), which are the dominant contribution of the unpolarised factors (solid). In three-body decays (right), there are two different scale factors for purely leptonic decays, noted as $\ell_\alpha \rightarrow \ell_\beta$: if the decay is mediated by $|U_{\beta N}|^2$, for which the $h = -1$ (dashed) and the $h = +1$ (dotted) components are comparable, and if the decay is mediated by $|U_{\alpha N}|^2$, for which $h = -1$ dominates over the $h = +1$ (dotdashed). In both cases, the two parts sum up to the same quantity (solid). The kaon decays are also divided in $h = -1$ (dashed) and $h = +1$ (dotted) components; $\tau^+ \rightarrow \nu\pi^+\pi^0$ is studied only at the phase space level.

flavours (muon and tau). The effect is particularly dramatic when the mass difference between parent meson and charged lepton widens, as it happens with the electron decay of D_s , the enhancement of which is around 10^6 for neutrino masses near 1 GeV.

The scale factor \mathcal{K}_h for leptonic decays of a pseudo-scalar meson P into neutrinos with helicity h , is given by the analytic expression:

$$\mathcal{K}_{\pm}^{P,\alpha}(m_N) = |U_{\alpha N}|^2 \frac{\lambda^{\frac{1}{2}}(1, \xi_N^2, \xi_{\ell_\alpha}^2) [\xi_{\ell_\alpha}^2 + \xi_N^2 - (\xi_N^2 - \xi_{\ell_\alpha}^2)^2 \pm (\xi_N^2 - \xi_{\ell_\alpha}^2) \lambda^{\frac{1}{2}}(1, \xi_N^2, \xi_{\ell_\alpha}^2)]}{2\xi_{\ell_\alpha}^2 (1 - \xi_{\ell_\alpha}^2)^2}, \quad (6.32)$$

where λ is the Källén function:

$$\lambda(a, b, c) = (a - b - c)^2 - 4bc,$$

and $\xi_i = m_i/m_X$ is the mass ratio of the final state particle i over the parent particle mass. When summing over the helicity states, the resulting factor coincides with the one computed in Ref. [?]:

$$\mathcal{K}^{P,\alpha}(m_N) = \sum_{h=\pm 1} \mathcal{K}_h^{P,\alpha}(m_N) = |U_{\alpha N}|^2 \frac{\lambda^{\frac{1}{2}}(1, \xi_N^2, \xi_{\ell_\alpha}^2) [\xi_{\ell_\alpha}^2 + \xi_N^2 - (\xi_N^2 - \xi_{\ell_\alpha}^2)^2]}{\xi_{\ell_\alpha}^2 (1 - \xi_{\ell_\alpha}^2)^2}.$$

In order to understand the effect of Eq. (6.32), it is convenient to define the fraction of neutrinos produced with a certain helicity as

$$S_{\pm} = \frac{\mathcal{K}_{\pm}^{P,\alpha}}{\mathcal{K}_{+1}^{P,\alpha} + \mathcal{K}_{-1}^{P,\alpha}} = \frac{1}{2} \left[1 \pm \frac{(\xi_N^2 - \xi_{\ell_\alpha}^2) \lambda^{\frac{1}{2}}(1, \xi_N^2, \xi_{\ell_\alpha}^2)}{\xi_{\ell_\alpha}^2 + \xi_N^2 - (\xi_N^2 - \xi_{\ell_\alpha}^2)^2} \right].$$

In the limit of a massless neutrino, i.e. $\xi_N \rightarrow 0$, the fractions are $S_+ \rightarrow 0$ and $S_- \rightarrow 1$, as expected: all neutrinos are produced with a negative helicity. The opposite is true when the charged lepton is in the massless limit, and the neutrinos are produced with a positive helicity.

The only two-body decay of a lepton considered in this work is $\tau \rightarrow \nu_\tau \pi$, and the scale factor is:

$$\mathcal{K}_{\pm}^{\tau,\pi}(m_N) = |U_{\tau N}|^2 \frac{\lambda^{\frac{1}{2}}(1, \xi_N^2, \xi_\pi^2) [(1 - \xi_N^2)^2 + \xi_\pi^2 (1 + \xi_N^2) \mp (1 - \xi_N^2) \lambda^{\frac{1}{2}}(1, \xi_N^2, \xi_\pi^2)]}{2(1 - \xi_\pi^2)^2}. \quad (6.33)$$

The structure is similar to the scale factor for pseudo-scalar meson two-body decays, given in Eq. (6.32), and analogous considerations as above can be deduced. This is explained by crossing symmetries, as the matrix element of the process is the same. In this case, however, the positive helicity component does not lead to any enhancement before the phase space cut-off.

The effect of the scale factors as a function of the neutrino mass can be appreciated in Fig. 6.2, where not only helicity terms are corrected, resulting in an enhancement of the production, but also the phase space is properly adjusted.

6.4.2 Three-body decays

Scale factors for three-body decays are defined in the same way as two-body decay ones. Because of the different number of degrees of freedom, the helicity of the outgoing neutrinos is not fixed by the spin of the parent particles. Hence, these factors are not responsible for any enhancement in the decay rate, but they only quench the process as the neutrino mass upper limit is approached (see Tab. 6.2). The scale factors have nonetheless distinct behaviours depending on the helicity state involved. Their behaviour is plotted as a function of the heavy neutrino mass in Fig. 6.2.

The decay of a charged lepton (antilepton) of flavour α to a charged lepton (antilepton) of flavour β can be proportional to either $|U_{\alpha N}|^2$ or $|U_{\beta N}|^2$, producing a heavy Dirac neutrino (antineutrino) in the first case or an antineutrino (neutrino) in the second case. If the neutrino is Majorana, the decay can occur via both mixing matrix elements because lepton number can be violated. Decays of muons and taus yield massive neutrinos with the following decay rate

$$\Gamma_{\pm}(\ell_{\alpha}^{+} \rightarrow \ell_{\beta}^{+} \nu N) = \frac{G_F^2 m_{\alpha}^5}{192\pi^3} \left[|U_{\alpha N}|^2 I_{\ell}^{\pm}(\xi_N^2, \xi_{\ell_{\beta}}^2, 0) + |U_{\beta N}|^2 I_{\bar{\ell}}^{\pm}(0, \xi_{\ell_{\beta}}^2, \xi_N^2) \right], \quad (6.34)$$

where the integrals $I_{\ell, \bar{\ell}}(x, y, z)$ are given in Appendix 6.8. The helicity decompositions in I_{ℓ} and $I_{\bar{\ell}}$ are different, but the spin-averaged decay width is the same.

Neutral and charged kaons produce neutrinos in three-body semi-leptonic decays. Both of them can decay into either a muon or an electron and a charged pion if the decaying kaon is neutral or a neutral pion if the kaon is charged. The decay width of a pseudo-scalar meson h_1 to a lighter meson h_2 is given by

$$\Gamma_{\pm}(h_1^{+,0} \rightarrow h_2^{0,+} \ell_{\alpha}^{+} N) = \frac{G_F^2 m_h^5}{128\pi^3} |U_{\alpha N}|^2 |V_{q\bar{q}}|^2 I_{h_1}^{\pm}(\xi_{h_2}^2, \xi_{\ell_{\alpha}}^2, \xi_N^2). \quad (6.35)$$

The integral $I_h(x, y, z)$ is reported in Appendix 6.8 and consists of a combination of kinematic elements with terms of hadronic form factors as coefficients. The scale factor was checked numerically against the result of Ref. [?].

The final three-body decay studied in this work is $\tau^{+} \rightarrow \bar{\nu}_{\tau} \pi^{+} \pi^0$, however this channel is introduced only at the phase space level. The scale factors for the two helicity components are therefore assumed to be identical, $\mathcal{K}_{\pm} = \frac{1}{2}$, such that the neutrino flux sub-component coming from this decay consists of equal number of heavy neutrinos with helicity $h = +1$ and $h = -1$.

6.5 Simulation of events at DUNE ND

DUNE [?] is a long-baseline oscillation experiment that will study neutrino physics in great detail, focusing mainly on the determination of the CP violating phase, δ_{CP} , of the mass ordering, and on the

precision measurement of other oscillation parameters, in particular θ_{23} . These goals can be achieved thanks to both an intense neutrino beam and a high-resolution Far Detector (FD), consisting of a 40 kt Liquid Argon Time Projection Chamber (LArTPC), situated 1300 km from the beam target. The drift velocity of ionised electrons in LAr, typically of the order of cm/μs, can be controlled with sufficient precision, by tuning the electric field, to result in high spatial resolution for event reconstruction [?]. A very sensitive FD alone, however, is not enough due to numerous uncertainties on neutrino flux and cross sections. A smaller and closer detector, called Near Detector (ND), is therefore adopted to normalise the flux of neutrinos reaching the FD and to help cancel out many of the neutrino-nucleon cross section systematics.

The DUNE ND will be placed 574 m from the target. Its final design has not been finalised yet, but it will likely be a hybrid concept, consisting of a small LArTPC placed in front of a magnetised high-pressure gaseous TPC. This module is complementary to the front detector, controlling escaping or below-threshold particles from the LArTPC, but is also capable of performing standalone measurement. For its versatile nature, it is called Multi-Purpose Detector (MPD). The sub-system LArTPC/MPD will be movable inside the ND hall—following the DUNE-PRISM concept—for better profiling the neutrino flux at different angles. There will be a third module, a 3D Scintillation Tracker (3DST), on-axis, to monitor the stability of the beam flux and neutron contamination. Currently, the proposed fiducial volume for the LArTPC module is 24 m³ (around 35 t of LAr), employing the ArgonCube technology [?], whereas the design for the MPD is based on the TPC in ALICE [?], a cylinder of 100 m³ with gas at a pressure of 10 atm and a fiducial mass of 1 t. The 3DST is designed to have a fiducial mass of around 8.7 t of plastic scintillating material and wavelength shifting plates. For this analysis, we take only in account the two core sub-detectors, the LArTPC and the MPD. The main difference between these two ND modules is that the gaseous TPC has a larger volume than the LArTPC. This feature is favourable for studying rare events, like heavy neutrino decays, because more neutrinos enter the fiducial volume. Furthermore, the lower density of the MPD helps reduce the number of neutrino scattering events, which are background to rare signatures. Apart from volume and density differences and relative positions in the detector hall, we treat the two ND units as with similar detection performances, on-axis, and do not take in account the magnetisation of the gaseous TPC.

Thanks to its proximity to the accelerator, the ND will be exposed to an extremely intense neutrino beam, with a flux peak around five million times greater than at the FD. The Long Baseline Neutrino Facility (LBNF) at Fermilab will deploy a very energetic beam of protons, extracted from the Main Injector (MI) and delivered to a graphite target. The collision produces secondary particles, which are collimated by a focusing horn system and then decay forming a neutrino beam. Assuming an 80 GeV proton beam at 1.2 MW for the first six years and at 2.4 MW for a second set of six years [?], the ND will collect in both neutrino and antineutrino mode a total of 2.65×10^{22} POT over the runtime of the experiment. In this work we consider only the beam in the neutrino mode configuration, which

	PS191	DUNE ND	SBND	NA62	SHiP
Baseline	128 m	574 m	110 m	220 m	60 m
Volume	216 m ³	124 m ³	80 m ³	750 m ³	590 m ³
Energy	19.2 GeV	80 GeV	8 GeV	400 GeV	400 GeV
POT	0.86×10^{19}	1.32×10^{22}	6.6×10^{20}	3×10^{18}	2×10^{20}
Exposure	1.0	193.5	16.1	8.5	5820

Tab. 6.3: Comparison between experiments mentioned in this work. The exposure is defined as $\text{POT} \times \text{Energy} \times \text{Volume} \times \text{Baseline}^{-2}$ with respect to PS191, where “Energy” is the proton beam energy. The NA62 and SHiP experiments are not directly comparable with SBND and DUNE ND, in that different technologies are involved; the RICH detectors are adopted as fiducial volume for NA62, whereas for SHiP, we estimate the volume as the cone contained in the “hidden sector” vacuum vessel. The volume is a driving feature in the definition of the total exposure and it is of utter importance for searches of decay-in-flight events.

corresponds to half of the total runtime, or 1.32×10^{22} POT. The same study of this article can be applied equally to the beam in reversed horn current configuration, but its details are not available to us. Including the analysis for the beam in antineutrino mode should result in an increment on the overall sensitivity, approximately a factor of two better.

A summary of the features of the ND system is reported in Tab. 6.3, where it is compared to other beam dump experiments: PS191 [? ?], SBND which is the detector of the SBN programme with the best sensitivity to HNL [?], NA62 [?], and SHiP [?]. We define the total exposure of the experiment as the proton accelerator beam power, integrated over the total run time, and scaled by the volume of the detector over its baseline squared. The beam power times the run time corresponds to the number of protons on target (POT) times the proton energy. With this definition, an exposure twelve times bigger is expected for the DUNE ND system with respect to SBND, and around two hundred times bigger than PS191. The NA62 and SHiP experiments have a different design and are not directly comparable to TPC and tracker experiments, but we report them here for thoroughness. The estimated exposure of NA62 is limited by its number of POT and by just one year of data taking; despite this fact, the experiment is optimised to study kaon decays and has good sensitivity to HNL [?]. The SHiP experiment presents an exposure thirty times bigger than DUNE ND, but the detector is specifically designed to search for BSM physics, including heavy neutrinos [?] (see also Ref. [?]). The decay-in-flight search hugely benefits from its 50 m long decay vessel and short baseline.

On the collider physics frontier, the FASER experiment [?] will perform a dedicated search for extremely weakly-interacting particles, like HNLs for which it presents interesting sensitivity [?]. The detector consists of a 10 m cylindrical decay volume located 480 m downstream of the ATLAS interaction point.

Fig. 6.3: The prediction of neutrino fluxes, in neutrino mode, divided by parentage at the ND are shown above, normalised to 10^{20} POT. The ν_e component (top left) predominately originates from μ^+ decays; kaon decays are responsible for the high energy part of the spectrum. The ν_μ component (top right) obtains its main contribution from π^+ decays at low energies, whereas the K^+ decays are accountable for the long tail of the spectrum. Contributions from D_s^+ decay are out of scale for both ν_e and ν_μ . The distribution of the $\bar{\nu}_\mu$ component (bottom left) is due to negative charged secondary particles which are not successfully deflected by the horn system; the muon contribution is much more relevant than for the ν_μ component. The ν_τ component (bottom right) is only sourced from D_s decays and presents a prominent peak at low energies, whereas the $\bar{\nu}_\tau$ are produced in τ^+ lepton decays. The dotted black line is the total $\bar{\nu}_\tau$ component of the flux.

Fig. 6.4: The fluxes of heavy neutrinos from $D_s^+ \rightarrow \tau^+ N$ (left) are presented for different neutrino masses and normalised to 10^{20} POT at the ND. Only phase space effects are considered here. For each different value of the neutrino mass, information on the start and end point of the spectrum and the peak of the flux are extracted and used to reshape the ν_τ spectrum. We show the distortion factors used in the scaling process for the channel producing $\bar{\nu}_\tau$: the energy range normalised to 20 GeV (middle) and the inverse of the peak re-scaling (right).

6.5.1 Flux prediction

In order to implement our analysis, the various components of the flux by parentage must be known separately. We study only the beam operating with a forward horn current, which selects positively charged secondary particles and results in a beam dominantly made of neutrinos with a smaller component of antineutrinos. The flux predictions for ν_e , ν_μ , and $\bar{\nu}_\mu$, provided by Ref. [?] for the reference beam, are shown in Fig. 6.3 subdivided in their parent components. The ν_μ flux is the dominant component and is principally originated by pion decays, whilst its long tail comes from kaon decays. Unsuccessfully deflected negative particles, like π^- or K^- , and the μ^+ are the main contributors to the $\bar{\nu}_\mu$ components, and ν_e comes predominately from the muon and both K^+ and K^0 decays. We consider only the energy range $E < 20$ GeV, because it is the most intense region of the flux and, as it will be explained in Section 6.5.3, the most relevant for this study.

We highlight here the fact that we expect also an albeit-small flux of HNLs with masses above the kaon one. This could be inferred from the ν_τ flux, but this is not available in the literature. In fact, the lightest meson with an interesting decay width to tau neutrinos is the charmed-strange meson D_s^+ , which has a mass $m_{D_s} = 1968.34 \pm 0.07$ MeV [?]. It decays into $\tau^+ \nu_\tau$ with a branching ratio of 5.48 ± 0.23 %. HNL with masses above the K^0 can be produced via the tau mixing, but more importantly via the muonic and electronic ones which are enhanced, as shown in Section 6.4. The meson D^+ also decays into $\tau^+ \nu_\tau$, but being lighter than the D_s^+ , the decay is disfavoured by the smaller phase space, with a branching ratio 50 times smaller. This meson presents three-body decay channels into ν_e and ν_μ with much higher branching ratio, but there is no enhancement for such channels into HNL, as explained in Section 6.4, and so these subdominant components are not taken in account in the present study.

The proton beam has a relatively low energy for producing charm quarks with a high cross-section, so the prediction of ν_τ has not been carried out by the collaboration to the best of our knowledge. For the reasons stated above, we make a prediction for the D_s^+ production by an 80 GeV proton beam hitting a fixed graphite target. The distribution at the production site will be then used to estimate the ν_τ flux at the ND system. In the literature, the following parametrisation has been successfully used to describe the charm meson production in proton-proton collision in the Centre of Mass frame [?]

$$\frac{d^2\sigma}{dx_F dp_T^2} \sim (1 - |x_F|)^n e^{-bp_T^2}, \quad (6.36)$$

where $x_F = 2p_z/\sqrt{s}$, with p_z the longitudinal momentum in the CM frame. The parameters n and b were fitted from the E769 experiment and found to be $n = 6.1 \pm 0.7$ and $b = 1.08 \pm 0.09$ [?]. We assume that the D_s^+ meson production at the target follows the same distribution. With the help of a Monte Carlo simulation, we generate the D_s^+ four-momenta starting from Eq. (6.36) and simulate the meson decay and the subsequent tau decays. A key simplification here is that because of the short lifetime of the D_s^+ and τ^+ , of the order of 10^{-13} s, their path is not affected by the horn system nor by interactions with other accelerator components. This results in no focusing of these secondary particles, and so only neutrinos emitted within the geometric acceptance of the ND are considered to form the ν_τ and $\bar{\nu}_\tau$ spectrum. The overall normalisation comes from an open charm calculation (see Appendix 6.10 for details): the number of D_s^+ per POT is found to be $(2.8 \pm 0.2) \times 10^{-6}$. The result of the simulation is reported in the bottom right panel of Fig. 6.3, where the different contributions to the ν_τ spectrum are shown. Thanks to the large number of POTs in DUNE, the total number of D_s^+ mesons produced is comparable to other dedicated experiments [?]; however, the beamline design is not optimised for heavy mesons production and the ν_τ flux seen at the ND is strongly attenuated.

Having knowledge of the parent meson distribution, we directly simulate the production of nearly-sterile neutrinos from the D_s decays. The spectrum of heavy neutrinos is distorted when their mass approaches the various phase space thresholds, which appears as a further enhancement of the flux. This is because heavier neutrinos are more easily boosted inside the geometric acceptance of the detector. Besides the peak height, the start and the end point of the energy flux are also affected, as illustrated in Fig. 6.4. We take these effects in account, modifying the scaled neutrino flux using information retrieved by the ν_τ and $\bar{\nu}_\tau$ simulation.

6.5.2 Background evaluation

The number of SM neutrino–nucleon interactions expected at the DUNE ND, without considering detector effects, is calculated by integrating the Charged Current (CC) and Neutral Current (NC) total cross sections multiplied by the light neutrino spectrum $d\phi_\nu/dE$:

$$\mathcal{N}_{\text{tot}} = \mathcal{N}_{\text{CC}} + \mathcal{N}_{\text{NC}} = \mathcal{N}_{\text{target}} \int dE [\sigma_{\text{CC}}(E) + \sigma_{\text{NC}}(E)] \frac{d\phi_\nu}{dE}, \quad (6.37)$$

	CC events			NC events		
	Per tonne	Ratio	Rate (Hz)	Per tonne	Ratio	Rate (Hz)
ν_e	3.0×10^3	75.6 %	6.6×10^{-3}	1.0×10^3	24.4 %	2.1×10^{-3}
ν_μ	240×10^3	75.2 %	530×10^{-3}	79.0×10^3	24.8 %	170×10^3
$\overline{\nu}_\mu$	17.8×10^3	70.9 %	40×10^{-3}	7.3×10^3	29.1 %	16×10^{-3}
ν_τ	7.4×10^{-6}	17.4 %	1.6×10^{-11}	3.5×10^{-5}	82.6 %	7.7×10^{-11}
$\overline{\nu}_\tau$	2.1×10^{-5}	45.3 %	4.7×10^{-11}	2.6×10^{-5}	54.7 %	5.7×10^{-8}

Tab. 6.4: The expected rates for CC and NC interaction in the near detector are presented here, normalised to 10^{20} POT. The values were computed starting from Eq. (6.37), convolving the fluxes of Fig. 6.3 with the CC and NC cross section predictions from GENIE [?]. Detector efficiencies are not applied. The first columns show the total number of events per tonne of argon, the second ones the proportion of CC or NC events with respect to the totality, and the last columns the event frequencies assuming 2.205×10^{14} POT/s.

where $\sigma_{\text{CC}}(E)$ and $\sigma_{\text{NC}}(E)$ are the cross section predictions in argon calculated with GENIE [?], and N_{target} is the total number of Ar targets. The event rates are shown in Tab. 6.4. It turns out that less than one ν_τ event is expected in the total run of the experiment. As a comparison, the number of ν_μ events will be 10^{10} times higher. This confirms the expectations that the ν_τ component of the flux is negligible for standard oscillation physics in DUNE ND. On the other hand ν_τ appearance is expected at the FD.

These neutrino scatterings occurring within the fiducial volume of the detector could mimic the rare signal of neutrino in-flight decays, as some final state particles are common to both processes. A good estimate of the number of possible background events for each discovery channel is very important, since it dictates the true sensitivity of the experiment. We restrict our conservative background analysis to decay modes available for neutrino masses below m_{K^0} , being these the channels with the best discovery potential. They are $N \rightarrow \nu e^+ e^-$, $\nu e^\pm \mu^\mp$, $\nu \mu^+ \mu^-$, $\nu \pi^0$, $e^\mp \pi^\pm$, and $\mu^\mp \pi^\pm$. Particles are typically tagged by studying the topology of the tracks and the energy loss dE/dx in the active medium, but instead of dealing with a full detector simulation, we perform a fast Monte Carlo analysis, using as input neutrino–nucleon scattering events in argon generated by the neutrino event generator GENIE [?]. The tracks are randomly placed inside the ND system and then smeared according to a normal distribution centred on the simulated value of energy/momentum; particles with a kinetic energy above the detection threshold are then assumed to be reconstructed. The relative position between the two detectors is taken into account, in that particle tracks exiting the LArTPC end entering the FGT are reconstructed as a single track. Escaping or partially reconstructed tracks are not discarded, but treated with a different energy/momentum resolution: the initial particle energy can be estimated, with some limitations, thanks to the energy dependence of the mean energy loss during the particle propagation. We then implement possible sources of background mis-identification which are channel specific. Detector resolutions and thresholds, from Ref. [?] for both parts of the ND, are summarised in Tab. 6.5.

Particle	Threshold	σ_{rel}	σ_θ
EM	30 MeV	$15\%/\sqrt{E} \oplus 2\%$	1°
Hadron	50 MeV	$30\%/\sqrt{E} \oplus 5\%$	5°
Muon	30 MeV	5% or 30% of $ \mathbf{p} $	1°
Pion	100 MeV	5% or 30% of $ \mathbf{p} $	1°

Tab. 6.5: The table lists detection thresholds and energy/momentum and angular resolutions used in the fast MC, where “EM” delineates electro-magnetic showers and “Hadron” any other charged particle which is neither a lepton nor a pion. The momenta of pions and muons are smeared according to the containment of their tracks. If more than 95 % of their track is reconstructed then the relative resolution on the momentum is 5 %, otherwise a resolution of 30 % is assumed.

A strong discriminant for background events is the presence of protons, neutrons, and other hadrons in the final states, which are the results of the nucleus recoil of the neutrino interaction. If hadronic activity is reconstructed as an interaction vertex, then the event is clearly originated by SM neutrino–nucleon scattering and tagged as background. In the case this does not happen, for instance when the hadrons are below threshold, the multiplicity of final state particles becomes fundamental to distinguish signal events from intrinsic background. However, this background can be worsened by mis-identification of certain tracks.

The main background to the pseudo-scalar meson channels, $N \rightarrow \ell^\mp \pi^\pm$, are resonance ν_e or ν_μ –CC interaction with single pion production or incoherent and deep inelastic scatterings in which only a pair $\ell\pi$ is detected. Three-body lepton decays suffers from mis-identification of additional pions and photons emitted in CC neutrino scatterings which are mistaken for charged leptons. Despite having a similar mass, pion and muon tracks differ on average in length, as the meson track often culminates in a hadronic shower. In our implementation of the detector effects, if no hadronic shower is detected and the track length is longer than two metres, the pion is identified as a muon. Electromagnetic shower induced by photons are identified by looking at the vertex displacement and at the dE/dx , which is twice as large as the energy loss for e^\pm . If a photon converts within two centimetres from the interaction point, and either the electron or the positron of the pair is below threshold, the photon is reconstructed as a single electron. A pair of electrons with a small separation angle, less than 3° , is tagged as an electron-positron pair and the parent photon is reconstructed. The main source of photons comes from the decay of the neutral pion, which is abundantly produced in neutrino–nucleon interactions. Certain hadronic transitions from secondary particles of deep inelastic scatterings also emit gammas. If a pair of photons shows an invariant mass comparable with the π^0 mass, the parent pion is identified. Interactions in which multiple neutral pions are produced, but only a pair of photons is detected and reconstructed, can be background to the $N \rightarrow \nu\pi^0$ channel. The background events surviving particle identification are between 5 % down to 0.01 % of the processed events, the rejection of which strongly depends on the analysed channel.

The channels which open up for masses above the kaon mass are more challenging from an experimental point of view. The final state particles of these modes are mostly neutral pseudo-scalar mesons, which decay electromagnetically, or vector mesons, which usually decay into a multi-state of lighter mesons, depending on the initial flavour content, sometimes accompanied by photon emission. The correct identification of these short-lived states is non trivial. For very high masses, also τ leptons are yielded, but their precise reconstruction requires *ad hoc* techniques. These tasks are beyond the scope of the analysis presented here and are best left to the collaboration superior simulation tools. We also do not consider cosmogenic background, even though a rate of 2.7 Hz/m^2 cosmic rays is expected at the ND hall [?], which has very little over burden. Given an area of a few square meters, the number of cosmic rays per drift window can be non-negligible [?], but rejection techniques are being developed with good signal efficiencies [?].

6.5.3 HNL decay events and signal efficiency

Except for N decaying into three neutrinos, all the other decay channels are in principle detectable. For a given visible decay mode d , the number of signal events is

$$\mathcal{N}_d = \int dE \Pi_d(E) W_d(E) \frac{d\phi_N}{dE}, \quad (6.38)$$

where $d\phi_N/dE$ is the number of heavy neutrinos expected at the ND, computed in the way described in Section 6.4. The function $\Pi_d(E)$ accounts for the probability of a heavy neutrino of energy E to decay inside the ND after covering the baseline distance L . It is expressed in the following form:

$$\Pi_d(E) = e^{-\frac{\Gamma_{\text{tot}}L}{\gamma\beta}} \left(1 - e^{-\frac{\Gamma_{\text{tot}}\lambda}{\gamma\beta}}\right) \frac{\Gamma_d}{\Gamma_{\text{tot}}}, \quad (6.39)$$

where λ is the length of the ND, Γ_d the decay rate for the channel d and Γ_{tot} the total decay rate. The total effect of Π_d is to favour low-energy bins of the neutrino spectrum for which the relativistic factor $\gamma\beta$ is small.

The term $W_d(E)$ is a signal efficiency factor, estimated as the binned ratio of the true N energy spectrum after and before a background rejection procedure. The latter is a process aiming to further reduce the number of background events still present after particle identification. It consists of simple data selection cuts optimised to reject the background while minimising the loss of signal events, exploiting differences in the energy and angular distributions of signal and background events. The HNL decays inside the detector are simulated by a custom Monte Carlo code and the tracks are processed in the same way as it is done for background events (see Section 6.5.2). The resulting signal efficiency therefore embeds also detector effects. If no background is expected for the channel d , there is no need for applying any rejection procedure and so the signal efficiency is maximal, i.e. $W_d(E) = 1$ at all energies. The final number of background events \mathcal{B}_d and the number of signal events \mathcal{N}_d are eventually used to build the Confidence Level (C.L.) regions of sensitivity (see Section 6.6). We leave a more detailed

discussion on the background reduction cuts in Appendix 6.11, where we report the rates of background reduction and signal selection for all decay channels of both Majorana and Dirac neutrinos of a given mass. We note that the Dirac neutrino decays generally have a lower signal efficiency, between 5% and 10% less, compared to a Majorana state of the same mass. This is a consequence of certain combinations of production and decay modes which are forbidden for Dirac neutrinos, as they would lead to LNV. The final true energy distributions of Majorana and Dirac neutrinos can therefore be different. When looking at the NC decay $N \rightarrow \nu\pi^0$, the difference in signal efficiency is almost recovered, thanks to the angular dependence of Dirac neutrino decays which makes it more distinguishable from background.

6.6 Sensitivities of DUNE ND

We present here sensitivity regions for the discovery of heavy neutrino decays for a total amount of 1.32×10^{22} POT collected with the beam in neutrino mode. All the regions are estimated at the 90 % C.L. in rejecting the null hypothesis, by which no HNL decays are seen ($\sigma = 0$), but only background events b are expected. For a specific channel d , the probability of observing n events with a signal mean $\sigma = \mathcal{N}_d$ and background $b = \mathcal{B}_d$ (see Section 6.5.3) follows a Poisson distribution

$$P(n|\sigma, b) = (\sigma + b) \frac{e^{-(\sigma+b)}}{n!} .$$

We employ the Feldman and Cousins method [?] to estimate the number of events needed in order to reject H_0 at the desired C.L.. For example, if no background is expected ($\mathcal{B}_d = 1$), an average of $n = 2.44$ events must be detected to reject H_0 with 90 % C.L. This criterion is used to define the sensitivity regions shown in this section, for both Majorana and Dirac neutrinos. It is found in every case that the MPD alone has a better sensitivity than the LArTPC, thanks not only to a larger volume, but also to a less dense medium which gives lower backgrounds. As the two modules are assumed to have the same detection performance, we present here a combined analysis of the two detectors, taking into account particle propagation between them. We do not consider charged identification capabilities of the ND, and therefore this information is washed out in presenting the sensitivity plots in this and next sections. Because of our charge-blind analysis, the number of events expected for Majorana neutrinos is twice as large as the number in the case of Dirac neutrinos, therefore the sensitivity to Dirac neutrino decays is a factor of two worse than the Majorana case. The limits reported here below refer to Majorana heavy neutrinos; the corresponding limit for which N is a Dirac fermion is easily retrieved by doubling the upper limit.

In Section 6.6.1, we show the constraint that DUNE ND can place on a simplified scenario in which a single mixing matrix element between HNL and active neutrinos dominates. We have also considered a scenario in which two mixings are dominant with respect to the third one, the results of which are presented in Section 6.6.2.

Fig. 6.5: The 90 % C.L. sensitivity regions for dominant mixings $|U_{eN}|^2$ (top), $|U_{\mu N}|^2$ (middle), and $|U_{\tau N}|^2$ (bottom) are shown. The solid lines correspond to the analysis before the background analysis, which is equivalent to a weighting factor $W_d = 1$ (see Eq. (6.38)). The dashed lines are drawn after our background analysis. The distinction between the fermionic natures are explained in the colour key.

6.6.1 Single dominant mixing

In this section, we present the sensitivity regions for the three mixings $|U_{eN}|^2$, $|U_{\mu N}|^2$, and $|U_{\tau N}|^2$, where we assume that just one mixing element dominates over the other two. The sensitivities for the decay channels $N \rightarrow \nu e^+ e^-$, $\nu e^\pm \mu^\mp$, $\nu \mu^+ \mu^-$, $\nu \pi^0$, $e^\mp \pi^\pm$ ($|U_{eN}|^2$ only), and $\mu^\mp \pi^\pm$ ($|U_{\mu N}|^2$ only) are reported in Fig. 6.5. The solid lines corresponds to a scenario in which zero background is assumed at the ND. A background study is done for these channels (see Section 6.5.2), to outline a more realistic sensitivity; the resulting regions are shown as dashed lines in Fig. 6.5. As we expect that further improvements to background reduction can be achieved with a dedicated analysis by the experimental collaboration, the final sensitivity will lie somewhere between the lines with and without backgrounds.

For both the electronic and the muonic mixings, the two-body semi-leptonic decay modes are the ones providing the best sensitivity for sufficiently heavy masses. With the channel $N \rightarrow e^\mp \pi^\pm$, the mixing can be constrained in the range $0.15 \text{ GeV} \lesssim m_N \lesssim 0.49 \text{ GeV}$ to be $|U_{eN}|^2 < 3 \times 10^{-9}$, with a minimum point $|U_{eN}|^2 < 7 \times 10^{-11}$ at $m_N \simeq 0.39 \text{ GeV}$. Including the background rejection, the limits are loosened by a factor of ~ 3.5 . The channel $N \rightarrow \mu^\mp \pi^\pm$ can constrain the mixing $|U_{\mu N}|^2 < 5.6 \times 10^{-10}$ in the mass range $0.25 \text{ GeV} \lesssim m_N \lesssim 0.39 \text{ GeV}$, with the best limit $|U_{\mu N}|^2 < 1.3 \times 10^{-10}$ at $m_N \simeq 0.35 \text{ GeV}$. In this case, the higher background and the worse signal efficiency reduce the bound up to a factor of ~ 5.6 . The NC decay $N \rightarrow \nu \pi^0$ is the channel most affected by background and with the worst signal efficiency: the limits are higher by a factor of ~ 9.0 for the electronic, ~ 8.2 for the muonic, and ~ 11.7 for the tau mixing. Assuming no background, instead, the constrains placed by this decay mode can be competitive, as the mixings are limited at best for $m_N \simeq 0.35 \text{ GeV}$ to be $|U_{eN}|^2 < 1.1 \times 10^{-10}$ and $|U_{\mu N}|^2 < 1.6 \times 10^{-10}$, and $|U_{\tau N}|^2 < 5 \times 10^{-7}$ between $0.9 \text{ GeV} \lesssim m_N \lesssim 1.3 \text{ GeV}$. There is no sensitivity to the channel $N \rightarrow \tau^\mp \pi^\pm$ because of the subdominant branching ratio and flux content.

The three-body lepton decays have a lower reach, but are more sensitive to masses above the kaon mass limit than the two-body semi-leptonic modes. The channel $N \rightarrow \nu e^- e^+$ is the only one that covers the whole mass range of interest and is the least affected by background reduction, with a factor less than 3. It can limit the electronic mixing down to $|U_{eN}|^2 < 2.6 \times 10^{-9}$ at $m_N \simeq 0.11 \text{ GeV}$, $|U_{eN}|^2 < 3.0 \times 10^{-10}$ at $m_N \simeq 0.39 \text{ GeV}$, and $|U_{eN}|^2 < 3.0 \times 10^{-9}$ at $m_N \simeq 1.6 \text{ GeV}$. The channels $N \rightarrow \nu \mu^- \mu^+$ and $\nu e^\pm \mu^\mp$, perform better with the muon mixing, despite suffering more from background rejection, between a factor of 8 for the muon mixing and up to a factor of 15 for the tau mixing. They respectively give the limits $|U_{\mu N}|^2 < 9.2 \times 10^{-10}$ at $m_N \simeq 0.37 \text{ GeV}$ and $|U_{\mu N}|^2 < 8.7 \times 10^{-8}$ at $m_N \simeq 1.5 \text{ GeV}$, and $|U_{\mu N}|^2 < 4.8 \times 10^{-10}$ at $m_N \simeq 0.36 \text{ GeV}$ and $|U_{\mu N}|^2 < 6.4 \times 10^{-8}$ at $m_N \simeq 1.6 \text{ GeV}$. The τ sector

Fig. 6.6: The 90 % C.L. sensitivity regions for dominant mixings $|U_{eN}|^2$ (top left), $|U_{\mu N}|^2$ (top right), and $|U_{\mu N}|^2$ (bottom) are presented for Majorana (solid lines) and Dirac (dashed lines) neutrinos. All the modes for which a background analysis was not performed are shown here. These channels become available only for masses above 500 MeV.

Fig. 6.7: The 90 % C.L. sensitivity regions for two dominant mixings $|U_{eN}^* U_{\mu N}|$ (top), $|U_{\mu N}^* U_{\tau N}|$ (middle), and $|U_{eN}^* U_{\tau N}|$ (bottom) are presented. All the modes considered in this work are shown here, but no background analysis is reported. As before, the solid lines correspond to the analysis with Majorana neutrinos, the dashed lines with Dirac neutrino.

can only be constrained by the two NC-mediated channels, which give very similar constraints near $m_N \simeq 1$ GeV, these being both $|U_{\tau N}|^2 < 1.2 \times 10^{-6}$.

A background study was not performed for all the other decay channels, which open up for masses above the K^0 mass, due to the fact that the final state particles need a more complex analysis. The sensitivities to these modes are shown in Fig. 6.6, and they can place some constraints to the mixing. All the channels peak in their sensitivity for masses between 1.3 and 1.8 GeV. The best limits obtained for CC decays are $|U_{eN}|^2 < 2.3 \times 10^{-9}$ from $N \rightarrow e^\mp \rho^\pm$ and $|U_{\mu N}|^2 < 6.2 \times 10^{-8}$ from $N \rightarrow \mu^\mp \rho^\pm$; among the NC decays $|U_{eN}|^2 < 3.7 \times 10^{-9}$ and $|U_{\mu N}|^2 < 1.0 \times 10^{-7}$ both from $N \rightarrow \nu \phi$. Even for these channels, there is no sensitivity to CC processes to the tau mixing, but interesting limits are set from $N \rightarrow \nu \omega$, $\nu \rho^0$ to be respectively $|U_{\tau N}|^2 < 1.8 \times 10^{-6}$, 8.8×10^{-7} .

6.6.2 Two dominant mixings

In this section we present the bounds in a scenario in which two mixing elements are comparable and dominant over the third one. This case complements the previous analysis in Section 6.6.1 as, by searching for HNL decays, the experiment can constrain certain combinations of the mixing elements. This can happen when the neutrino is produced via one mixing and decays via another one, or when both mixing elements play a role in production and decay. For instance, the decay $K^+ \rightarrow \mu^+ N$ yields heavy neutrinos with a flux proportional to $|U_{\mu N}|^2$, but they can afterwards decay into the channel $\nu e^+ e^-$ also via the electronic or the tau mixing. It is important to highlight that, in the case in which one mixing is responsible for the production and a different mixing for the decay, then number of events is proportional to the product of the mixings $|U_{\alpha N}| |U_{\beta N}|$ if the studied channel is CC-mediated. However, if the decay channel is also sensitive to a NC exchange, the number of events is instead proportional to $|U_{\alpha N}| \sqrt{|U_{\alpha N}|^2 + |U_{\beta N}|^2}$. In the remainder of this section, we will use the combination of two mixings represented by $|U_{\alpha N}^* U_{\beta N}|$ for comparing bounds and sensitivity plots.

The combinations of mixing terms is relevant to charged Lepton Flavour Violating (cLFV) decays or flavour changing neutral current processes which can be enhanced in presence of nearly-sterile neutrinos. For example, the well-known decay $\mu^+ \rightarrow e^+ \gamma$ has a branching ratio which is sensitive to extra neutrino states. This reads

$$\text{Br}(\mu^+ \rightarrow e^+ \gamma) = \frac{3\alpha}{32\pi} \left| \sum_i \hat{U}_{\mu i}^* \hat{U}_{ei} G\left(\frac{m_i^2}{M_W^2}\right) \right|, \quad (6.40)$$

where $G(x)$ is the loop function of the process [?]. The current upper limit is set by the MEG experiment to be $\text{Br}(\mu^+ \rightarrow e^+ \gamma) < 4.2 \times 10^{-13}$ [?]. Despite being one of the best constrained cLFV process, the bounds on $|U_{eN}^* U_{\mu N}|$ are not as good as the ones imposed by other processes, like $\mu \rightarrow eee$ or $\mu - e$ conversion on nuclei [?]. For instance, the constraint from conversion on Au is $|U_{eN}^* U_{\mu N}| < 1.6 \times 10^{-5}$ for HNL masses larger than 100 MeV [?]. The branching ratio of other cLFV channels, like $\tau \rightarrow e\gamma$ or $\tau \rightarrow \mu\gamma$ are not as well constrained and so the bounds achievable on the combination of heavy neutrino mixings are expected to be less stringent [? ?]. Stronger bounds come from study of three-body decays of charm and bottom mesons to charged leptons with different flavour and tau decays to pseudo-scalar mesons and a charged lepton: from the search for the decay $K \rightarrow e\mu\pi$ the bound $|U_{eN}^* U_{\mu N}| < 10^{-9}$ is reached for masses $150 \text{ MeV} \lesssim m_N \lesssim 500 \text{ MeV}$; the decays $\tau \rightarrow e\pi\pi$ and $\tau \rightarrow \mu\pi\pi$ set the limits $|U_{eN}^* U_{\tau N}|, |U_{\mu N}^* U_{\tau N}| < 5 \times 10^{-6}$ for the respective mass ranges $0.14 \text{ GeV} \lesssim m_N \lesssim 1.7 \text{ GeV}$ and $0.24 \text{ GeV} \lesssim m_N \lesssim 1.7 \text{ GeV}$ [?].

Instead of dealing with a three-dimensional parameter scan, we simplify the study by assigning the same value to the two mixing parameters under consideration. The number of events is then reported as a function of the neutrino mass and the combination $|U_{\alpha N}^* U_{\beta N}|$. The results for all channels considered in this work are shown in Fig. 6.7. The best constraints come again from two-body semi-leptonic decays for all mixing combinations, the lowest upper limits being $|U_{eN}^* U_{\mu N}| < 6.3 \times 10^{-11}$ at $m_N \simeq 0.37 \text{ GeV}$, $|U_{\mu N}^* U_{\tau N}| < 1.1 \times 10^{-10}$ at $m_N \simeq 0.35 \text{ GeV}$, and $|U_{\tau N}^* U_{eN}| < 7.4 \times 10^{-11}$ at $m_N \simeq 0.39 \text{ GeV}$. Amongst the three-body leptonic decay channels, $N \rightarrow \nu ee$ has the best sensitivity to masses $m_N < m_{K^0}$, but actually the mode $N \rightarrow \nu e^\mp \mu^\pm$ can be more constraining at higher masses. Regarding the channels available only above the kaon mass threshold, decays to pseudo-scalar mesons are the most sensitive between C processes, whereas the decay $N \rightarrow \nu \phi$ gives the best constraint of the NC-mediated channels.

6.7 Mass model constraints from DUNE ND

From the results presented in the previous section, we find that the DUNE ND will be sensitive to very low couplings for experimentally accessible mass values. These points of the parameter space corresponds to regions viable in some realisations of low scale neutrino mass models. In view of the discussion regarding seesaw models in Section 6.2, we perform a mass matrix random scan to define such regions of the parameter space. Following the previously introduced notation, we focus on three minimal ISS scenarios which predict a HNL with a mass accessible by the experiment and that satisfy the experimental evidence of neutrino oscillation [?]. In the first two cases, the heavy neutrino under study belongs to the lightest pseudo-Dirac pair of an ISS (2,2) and an ISS (2,3) realisation; the third scenario is an ISS (2,3) case in which the fourth Weyl state becomes a Majorana neutrino in the MeV–GeV region thanks to a high LNV parameter. The details of this analysis are reported in this section, together with the overall sensitivities of DUNE ND to heavy neutrino discovery and low scale mass models. A

comparison with future experiments is also included.

6.7.1 Mass model scan

We have randomly generated neutrino mass matrices and numerically diagonalised them. The structure of the mass matrix is a generalised version of an ISS:

$$\mathcal{M} = \begin{pmatrix} 0 & m_D^T & 0 \\ m_D & \mu_R & M_R^T \\ 0 & M_R & \mu_S \end{pmatrix}, \quad (6.41)$$

with two LNV submatrices, μ_R and μ_S . The number of physical parameters of a ISS (a, b) mass matrix is $n_p = 7a + b + 2ab$ [?]. We choose a basis in which m_D has complex entries but three of which are real, M_R is diagonal and real, and μ_S has a real diagonal without loss of generality. If the matrix entries respect the hierarchy $\mu_{R,S} \ll m_D \ll M_R$, the mass spectrum in the LNC limit is principally given by the diagonal values of M_R . We then perturb the matrix to achieve the three minimal ISS scenarios introduced above; the randomly generated mass matrix \mathcal{M} is then diagonalised using the Jacobi Singular Value Decomposition (SVD) as implemented in the Eigen library [?]. The Takagi decomposition,

$$\hat{U}^T \mathcal{M} \hat{U} = \text{diag}(m_1, m_2, m_3, \dots),$$

is retrieved starting from the SVD decomposition $\mathcal{M} = V \Sigma U^\dagger$, from which the singular values Σ are the non-negative square roots of the eigenvalues of $\mathcal{M}^\dagger \mathcal{M}$ and the unitary matrix is $\hat{U} = U \rho^\dagger$, where $\rho = (U^T V)^{\frac{1}{2}}$ is a unitary phase matrix.

Only matrices satisfying the current constraints on heavy neutral fermions are taken in account. The first requirement is that the eigenvalues must give the correct mass squared splittings compatible within 3σ with the measured values [?]. The condition of matching also the measured mixing angles is relaxed because the entries of the PMNS matrix, \mathcal{U} , are the result of the random structure of m_D and μ_S . Constraints on the unitarity of the mixing matrix are applied instead. The deviation from unitarity are quantified by the following Hermitian matrix:

$$\varepsilon_{\alpha\beta} \equiv |\delta_{\alpha\beta} - (\mathcal{U} \mathcal{U}^\dagger)_{\alpha\beta}| = \left| \sum_{i=4}^n \hat{U}_{\alpha i} \hat{U}_{\beta i}^* \right|. \quad (6.42)$$

The non-unitarity of the PMNS matrix has been assessed in various experiments, and the constraints depend upon the mass scale of averaged out neutrinos. For neutrino masses below the GeV scale, but heavy enough to decouple from flavour oscillations, non-unitarity effects are tested in neutrino oscillation experiment as an overall normalisation. If the neutrino mass is above the GeV scale, electroweak precision experiments provide strong constraints on non-unitarity. The constraints are summarised

below (from Ref. [? ? ?])

$$\varepsilon_{\alpha\beta} < \begin{pmatrix} 2.4 \times 10^{-2} & 1.3 \times 10^{-2} & 3.5 \times 10^{-2} \\ . & 2.2 \times 10^{-2} & 6.0 \times 10^{-3} \\ . & . & 1.0 \times 10^{-1} \end{pmatrix} \quad \text{if } 10 \text{ eV} \lesssim m_N \lesssim 1 \text{ GeV ,}$$

$$\varepsilon_{\alpha\beta} < \begin{pmatrix} 1.3 \times 10^{-3} & 1.2 \times 10^{-5} & 1.4 \times 10^{-3} \\ . & 2.2 \times 10^{-4} & 6.0 \times 10^{-4} \\ . & . & 2.8 \times 10^{-3} \end{pmatrix} \quad \text{if } m_N \gtrsim 1 \text{ GeV .}$$

The μ_R and μ_S entries of the ISS matrices naturally lead to lepton flavour and lepton number violating processes. The most constrained process is the decay rate of $\mu^+ \rightarrow e^+ \gamma$, the branching ratio of which is given in Eq. (6.40). The current upper limit on the branching ratio is 4.2×10^{-13} , but a future upgrade of the experiment foresees to reach a limit lower than 5×10^{-14} .

Heavy neutrinos in a ISS model also contribute to the neutrinoless double beta decay. The effective neutrino mass $m_{\beta\beta}$ receives further corrections with respect to the standard expression as

$$m_{\beta\beta} \simeq \left| \sum_i \hat{U}_{ei}^2 \frac{p^2 m_i}{p^2 - m_i^2} \right| \quad (6.43)$$

where $p^2 \simeq -0.015 \text{ GeV}^2$ is the typical virtual momentum of the exchanged neutrino. The contribution from masses above the 100 MeV scale drops as $1/m_i^2$ while it is constant for masses below [?]. It is interesting to note that the contributions given by pseudo-Dirac pairs are subject to partial cancellation, regulated by the LNV parameters. In the LNC limit, the cancellation is maximum and the paired states do not take part in the $0\nu\beta\beta$ process. The latest result from the KamLAND-Zen experiment [?] is interpreted as $m_{\beta\beta} < 61 \text{ meV}$.

We find, for the first two ISS scenarios, that the allowed ranges span in the space $m_D \sim 10^{[3,6]} \text{ eV}$, $M_R \sim 10^{[6,15]} \text{ eV}$, μ_S and $\mu_R \sim 10^{[-4,1]} \text{ eV}$. We check that each matrix generated respects the *naturalness condition* in the 't Hooft sense [?] and that the mass spectrum presents a mass state accessible by the DUNE experiment. For the third ISS case, large entries of the sub-matrix μ_S are necessary to give the Majorana state a mass that can be probed by the experiment. We find the ranges of $m_D \sim 10^{[3,10]} \text{ eV}$, $M_R \sim 10^{[7,15]} \text{ eV}$, $\mu_S \sim 10^{[4,9]} \text{ eV}$ to respect the constraints. The hierarchy and naturalness conditions are relaxed in this case. It is found that the block μ_R does not influence the final mass spectrum; it usually gives contribution to the light neutrino masses at the loop level, in a region below the GeV scale that has been already excluded by experiments. The resulting points in the space $(m_N, |U_{\alpha N}|^2)$ are clustered together and the regions defined are overlaid in Fig. 6.8. Any combination of mass and mixing element inside these areas can be justified by a valid neutrino mass matrix which can explain the light neutrino masses and survive the experimental constraints. The pseudo-Dirac pairs from the ISS (2,2) and ISS (2,3) scenarios give very similar regions, but Majorana states from the ISS (2,3) realisation can only be generated with very small couplings. A type I seesaw band, corresponding to light neutrino mass between 20 meV and 200 meV, is plotted as well for comparison.

Fig. 6.8: The 90 % C.L. sensitivity regions for dominant mixings $|U_{eN}|^2$ (top left), $|U_{\mu N}|^2$ (top right), and $|U_{\tau N}|^2$ (bottom) are presented combining results for channels with good detection prospects. The study is performed for Majorana neutrinos (solid) and Dirac neutrinos (dashed), assuming no background. The region excluded by experimental constraints (brown) is obtained by combining the results from PS191 [? ?], peak searches [19? ? ? ?], CHARM [?], NuTeV [21], DELPHI [20], and T2K [?]. The sensitivity for DUNE ND (black) is compared to the predictions of future experiments, SBN [?] (blue), SHiP [?] (red), NA62 [?] (green), and FASER [?] with 1 m radius. The shaded areas corresponds to possible neutrino mass models considered in this article: the simulations of the ISS (2,2) and ISS (2,3) models where the lightest pseudo-Dirac pair is the neutrino decaying in the ND (cyan); the ISS (2,3) scenario when the single Majorana state is responsible for a signal (magenta); the type I seesaw scenario with a neutrino mass starting from 20 meV to 0.2 eV (yellow).

6.7.2 Overall sensitivity

We define the overall sensitivity of DUNE ND to the discovery of HNL as the combination of the sensitivities to selected channels, presented in Section 6.6. These channels are $N \rightarrow \nu ee$, $\nu e\mu$, $\nu \mu\mu$, $\nu \pi^0$, $e\pi$, $\mu\pi$ and are preferred because of their good discovery prospect, for which backgrounds have also been studied. They all give strong sensitivities, especially for masses below 500 MeV. Their reach is due to high branching ratios and also to clean and well-defined signatures in the detector, allowing the background to be controlled with sufficient precision. The neutrino spectrum component coming from the D_s meson allows for weaker sensitivity to masses above the neutral kaon mass. We conducted the sensitivity study for both scenarios, in which either a Majorana or a Dirac neutrino is the decaying particle.

To appreciate the ND performance, we make a comparison with results of previous experiments, in particular PS191 [? ?], peak searches [19? ? ?], CHARM [?], NuTeV [21], DELPHI [20], and T2K [?]. We find that the DUNE ND can increase the bound on the electronic and muonic mixing elements for masses $m_N < m_{K^0}$ with respect to previous experiments. The constraint on the tauonic mixing is at least comparable with previous results. For masses above, for which neutrino production relies on charm meson decays, the existing bounds are improved for the electronic mixing and the tauonic mixing, while a conservative result can be achieved in the muonic case. We also overlay the prospects for the SBN programme [?], NA62 [?], and the proposed SHiP [?] and FASER [?] with 1 m radius. DUNE ND will give the best sensitivity for masses below the 500 MeV in all channels, but the tauonic one. However, anywhere the D_s meson production is involved, the experiment cannot outperform the predicted sensitivity of the SHiP experiment which will deploy a 400 GeV proton beam on a titanium-zinc-molybdenum alloy target, enhancing the production of charm and bottom mesons. NA62 gives better results for the $|U_{\mu N}|^2$ mixing, but DUNE has a better sensitivity to the electron and tau channels. FASER is comparable to NA62 in sensitivity, but it can reach regions of the parameter space beyond the 2 GeV limit to which DUNE is not sensitive.

We then compare the overall sensitivity to regions allowed by neutrino mass models. In the elec-

Fig. 6.9: One of the two ISS(2,3) realisations considered presents a Majorana state at masses comparable with SBL experiments. We show the results of the ISS(2,3) simulation (blue dots) for Δm_{41}^2 against combination of mixing angles and the experimental result at 90 % C.L.: $|U_{e4}|^2$ (left) compared to Super-Kamiokande and IceCube combined [?] and DANSS [?], $\sin^2 2\theta_{\mu e} = 4|U_{eN4}|^2|U_{\mu 4}|^2$ (middle) compared to KARMEN2, OPERA and MiniBooNE [?], and $|U_{\mu 4}|^2$ (right) compared to a combined ν_μ disappearance analysis [?]. Only the points generated by matrices which pass the experimental constraints are shown here.

tronic and muonic channels, DUNE ND will be sensitive to a large part of the pseudo-Dirac regions, corresponding to ISS(2,2) and ISS(2,3) models, part of which have been already excluded by past experiments. DUNE will close the gap and put to test type I seesaw parameters, especially for HNL masses between 200 and 500 MeV, starting to reach the region of ISS(2,3) with large lepton number violation. For the tauonic channel, the experiment will probe only a small portion of pseudo-Dirac pairs from ISS(2,2) and ISS(2,3) models. The sensitivity is not high enough to reach type I and Majorana state regions, which not even the dedicated experiment SHiP can.

The ISS(2,3) scenario in which the pseudo-Dirac pair is accessible by the experiment also predicts a light Majorana state, the mass of which is controlled by the small LNV perturbations. This entails the presence of a third mass splitting Δm_{41}^2 , which could give an active-sterile oscillation signature in short baseline experiments. In figure Fig. 6.9, the new mass splitting is plotted against the mixings $|U_{e4}|^2$, $|U_{\mu 4}|^2$ and the combination usually referred to as $\sin^2 2\theta_{\mu e} \equiv 4|U_{e4}|^2|U_{\mu 4}|^2$. The mass splittings generated in the matrix scan span from $\Delta m_{31}^2 \simeq 0.0025 \text{ eV}^2$ up to 10^4 eV^2 , and the squared mixings cover a large region, down to 10^{-14} for all the flavours. The reactor anomalies could be soon excluded at the 90 % C.L. by the DANSS experiment [?] and the allowed regions from LSND [?] and MiniBooNE [? ?] require values of $\sin^2 2\theta_{\mu e} \gtrsim 10^{-3}$. Given the results of the matrix scan, it is unlikely that one of the ISS(2,3) realisations considered in this work could link an heavy neutrino-like signal in DUNE ND and explain a short baseline anomaly at the same time, unless for sparse and very fine-tuned points.

6.8 List of integrals and identities

In presenting the differential and total decay rates in Section 6.3 and 6.4, we have used a series of simplifying integrals and functions of the particle masses. We report them jointly here. The letters x , y , and z denote squared ratios of masses, while s , t , and u are the corresponding Mandelstam variables for three body decays.

6.8.1 Decay widths

In [17], the following functions are used to express the total rates of two-body decays

$$\begin{aligned} I_1(x, y) &= \lambda^{\frac{1}{2}}(1, x, y) [(1-x)^2 - y(1+x)] , \\ I_2(x, y) &= \lambda^{\frac{1}{2}}(1, x, y) [(1+x-y)(1+x+2y) - 4x] , \end{aligned}$$

and the rate of three-body decays can be expressed in terms of two more functions [17],

$$I_1(x, y, z) = 12 \int_{\frac{(\sqrt{x}+\sqrt{y})^2}{(1-\sqrt{z})^2}}^{\frac{(1-\sqrt{z})^2}{(\sqrt{x}+\sqrt{y})^2}} \frac{ds}{s} (s - x - y) (1 + z - s) \lambda^{\frac{1}{2}}(1, x, y) \lambda^{\frac{1}{2}}(1, s, z) ,$$

$$I_2(x, y, z) = 24 \sqrt{yz} \int_{\frac{(\sqrt{y}+\sqrt{z})^2}{(1-\sqrt{x})^2}}^{\frac{(1-\sqrt{x})^2}{(\sqrt{y}+\sqrt{z})^2}} \frac{ds}{s} (1 + x - s) \lambda^{\frac{1}{2}}(s, y, z) \lambda^{\frac{1}{2}}(1, s, x) .$$

In this work we have introduced two differential generalisations of the two-body formulae,

$$I_1^\pm(x, y; \theta) = \frac{1}{4\pi} \lambda^{\frac{1}{2}}(1, x, y) \left[(1 - x)^2 - y(1 + x) \pm (x - 1) \lambda^{\frac{1}{2}}(1, x, y) \cos \theta \right] ,$$

$$I_2^\pm(x, y; \theta) = \frac{1}{4\pi} \lambda^{\frac{1}{2}}(1, x, y) \left[(1 + x - y)(1 + x + 2y) - 4x \pm (x + 2y - 1) \lambda^{\frac{1}{2}}(1, x, y) \cos \theta \right] .$$

Our expressions satisfy the normalisation conditions,

$$\int_0^{2\pi} d\varphi \int_{-1}^1 d\cos \theta I_1^\pm(x, y; \theta) = I_1(x, y) ,$$

$$\int_0^{2\pi} d\varphi \int_{-1}^1 d\cos \theta I_2^\pm(x, y; \theta) = I_2(x, y) .$$

We also note the following integrals which are necessary in deriving the total decay rate for the three-body leptonic modes,

$$\int ds_1 \int ds_2 (s_2 - \xi_3^2)(1 + \xi_4^2 - s_2) = \frac{I_1(0, \xi_3^2, \xi_4^2)}{12} , \quad (6.44)$$

$$\int ds_1 \int ds_2 (s_1 - \xi_4^2)(1 + \xi_3^2 - s_1) = \frac{I_1(0, \xi_4^2, \xi_3^2)}{12} , \quad (6.45)$$

$$\int ds_1 \int ds_2 2\xi_3 \xi_4 (s_1 + s_2 - \xi_3^2 - \xi_4^2) = \frac{I_2(0, \xi_3^2, \xi_4^2)}{12} , \quad (6.46)$$

where ξ_i have the same meanings of Eqs. (6.17) and (6.18).

6.8.2 Scaling factors for three body-decays

Three-body lepton decays can produce neutrinos in two ways, depending on whether the neutrino mixes with the initial or with the final flavour. The expressions presented in Section 6.4 make use of the following integrals:

$$I_\ell^\pm(x, y, z) = 12 \int_{\frac{(\sqrt{x}+\sqrt{y})^2}{(1-\sqrt{z})^2}}^{\frac{(1-\sqrt{z})^2}{(\sqrt{x}+\sqrt{y})^2}} \frac{ds}{s} (1 + z - s) \left[s - x - y \mp \lambda^{\frac{1}{2}}(s, x, y) \right]$$

$$\times \lambda^{\frac{1}{2}}(s, x, y) \lambda^{\frac{1}{2}}(1, s, z) ,$$

$$I_{\bar{\ell}}^\pm(x, y, z) = 12 \int_{\frac{(\sqrt{y}+\sqrt{z})^2}{(1-\sqrt{x})^2}}^{\frac{(1-\sqrt{x})^2}{(\sqrt{y}+\sqrt{z})^2}} \frac{ds}{s} \left[1 + z - s \mp \lambda^{\frac{1}{2}}(1, s, z) \right] (s - x - y)$$

$$\times \lambda^{\frac{1}{2}}(s, y, z) \lambda^{\frac{1}{2}}(1, s, z) .$$

When averaging over the helicity states, these two functions become identical and, because of symmetry crossing, also identical to the integral $I_1(x, y, z)$, expressed above.

In Section 6.4, the three-body decay rate of pseudoscalar meson requires the following integral:

$$I_h^\pm(x, y, z) = \int_{\frac{(\sqrt{x}+\sqrt{y})^2}{(1-\sqrt{z})^2}}^{(1-\sqrt{z})^2} ds \int_{t_-}^{t_+} dt [F^2 A^\pm(s, t) + G^2 B^\pm(s, t) - \text{Re}(F^* G) C^\pm(s, t)] ,$$

with $t_\pm = x + z + \frac{(1-s-z)(s-y+x) \pm \lambda^{\frac{1}{2}}(s, y, z) \lambda^{\frac{1}{2}}(1, s, z)}{2s}$,

where F and G are convenient combinations of hadronic form factors $f^{(h, h')}$. From lattice QCD considerations, form factors should carry the correct Clebsch-Gordan, but here we drop them as they are irrelevant when studying scale factors. The combinations F and G are

$$F = 2 f_+^{(h, h')}(u) = f_+^{(h, h')}(0) \left(1 + \lambda_+^{(h, h')} \frac{u}{x} \right) ,$$

$$G = f_+^{(h, h')}(u) - f_-^{(h, h')}(u) = f_+^{(h, h')}(0) \left[1 + \lambda_+^{(h, h')} \frac{u}{x} - (\lambda_+^{(h, h')} - \lambda_0^{(h, h')}) \left(1 + \frac{1}{x} \right) \right] ,$$

with λ parametrising the linear dependence [?] of the form factors with respect the momentum transfer between the two mesons, u , directly connected to the other Mandelstam variables, s and t :

$$u = 1 + x + y + z - s - t .$$

The values of $\lambda_{+,0}$ is determined experimentally [?]. The functions A , B , and C are

$$A^\pm(s, t) = \frac{1}{2}(1+y-t) \left[1 + z - s \mp \lambda^{\frac{1}{2}}(1, z, s) \right] - \frac{1}{2} \left[u - y - z \mp \lambda^{\frac{1}{2}}(u, y, z) \right] ,$$

$$B^\pm(s, t) = \frac{1}{2}(y+z)(u-y-z) + 2yz \mp (y-z) \frac{\lambda^{\frac{1}{2}}(u, y, z)}{2} ,$$

$$C^\pm(s, t) = z(1+y-t) + \left[y \pm \frac{\lambda^{\frac{1}{2}}(u, y, z)}{2} \right] (1+z-s) .$$

When summing over helicity states, the kinematic simplifies to

$$A(s, t) = (1+y-t)(1+z-s) - (u-y-z) ,$$

$$B(s, t) = (y+z)(u-y-z) + 4yz ,$$

$$C(s, t) = 2z(1+y-t) + 2y(1+z-s) .$$

6.9 Polarised $N \rightarrow \nu \ell_\alpha^- \ell_\beta^+$ distributions

6.9.1 Dirac ν_i

The coefficients for a Dirac neutrino decay are given by

$$\begin{aligned} C_1^\nu &= C_4^\nu = \sum_{\gamma=e}^\tau |U_{\gamma i}|^2 [\delta_{\alpha\beta} g_L^2 + \delta_{\gamma\alpha} (1 + \delta_{\alpha\beta} g_L)] , \\ C_2^\nu &= C_5^\nu = \delta_{\alpha\beta} g_R^2 \sum_{\gamma=e}^\tau |U_{\gamma i}|^2 , \\ C_3^\nu &= C_6^\nu = \delta_{\alpha\beta} g_R \sum_{\gamma=e}^\tau |U_{\gamma i}|^2 (\delta_{\gamma\beta} + g_L) , \end{aligned}$$

where the chiral couplings for charged leptons are given by $g_L = -\frac{1}{2} + \sin^2 \theta_W$ and $g_R = \sin^2 \theta_W$.

6.9.2 Dirac $\bar{\nu}_i$

The coefficients for the Dirac antineutrino decay—which involve some vital minus signs compared to the neutrino case—are given by

$$\begin{aligned} C_1^{\bar{\nu}} &= -C_4^{\bar{\nu}} = \delta_{\alpha\beta} g_R^2 \sum_{\gamma=e}^\tau |U_{\gamma i}|^2 , \\ C_2^{\bar{\nu}} &= -C_5^{\bar{\nu}} = \sum_{\gamma=e}^\tau |U_{\gamma i}|^2 [\delta_{\alpha\beta} g_L^2 + \delta_{\gamma\beta} (1 + \delta_{\alpha\beta} g_L)] , \\ C_3^{\bar{\nu}} &= -C_6^{\bar{\nu}} = \delta_{\alpha\beta} g_R \sum_{\gamma=e}^\tau |U_{\gamma i}|^2 (\delta_{\alpha\gamma} + g_L) , \end{aligned}$$

where the chiral couplings g_L and g_R have the same meaning.

6.9.3 Majorana N_i

The amplitude for Majorana decay is the sum of the Dirac neutrino and Dirac antineutrino amplitudes given above:⁵

$$|A_\pm|^2 = |A_\pm^\nu|^2 + |A_\pm^{\bar{\nu}}|^2 .$$

Crucially, this means that the coefficients in the isotropic terms are the sum of those for a neutrino and antineutrino while the coefficients in the angular terms are the difference, leading to cancellations. All in all, we find

$$|A_\pm|^2 = |A_0|^2 \pm |A_1|^2 ,$$

⁵In general, there are interference terms between “neutrino” and “antineutrino” diagrams; however all such contributions are suppressed by the mass scale of the outgoing light neutrino, which is taken to be zero in these calculations.

$$, \quad + \quad +$$

Fig. 6.10: These are the four diagrams contributing to the hard process in open charm production. The diagrams with gluons in the initial state interfere with each other giving rise to cross terms in the colour structure.

with the coefficients

$$\begin{aligned} C_1 &= C_1^\nu + C_1^{\bar{\nu}} = \sum_{\gamma=e}^{\tau} |U_{\gamma i}|^2 [(g_L^2 + g_R^2) \delta_{\alpha\beta} + \delta_{\gamma\alpha} (1 + \delta_{\alpha\beta} g_L)] , \\ C_2 &= C_2^\nu + C_2^{\bar{\nu}} = \sum_{\gamma=e}^{\tau} |U_{\gamma i}|^2 [(g_L^2 + g_R^2) \delta_{\alpha\beta} + \delta_{\gamma\beta} (1 + \delta_{\alpha\beta} g_L)] , \\ C_3 &= C_3^\nu + C_3^{\bar{\nu}} = 2 \delta_{\alpha\beta} g_R \sum_{\gamma=e}^{\tau} |U_{\gamma i}|^2 (\delta_{\alpha\gamma} + g_L) , \\ C_4 &= C_1^\nu - C_1^{\bar{\nu}} = \sum_{\gamma=e}^{\tau} |U_{\gamma i}|^2 [\delta_{\alpha\beta} (g_L^2 - g_R^2) + \delta_{\gamma\alpha} (1 + \delta_{\alpha\beta} g_L)] , \\ C_5 &= C_2^\nu - C_2^{\bar{\nu}} = - \sum_{\gamma=e}^{\tau} |U_{\gamma i}|^2 [\delta_{\alpha\beta} (g_L^2 - g_R^2) + \delta_{\gamma\beta} (1 + \delta_{\alpha\beta} g_L)] , \\ C_6 &= C_3^\nu - C_3^{\bar{\nu}} = 0 . \end{aligned}$$

Note that for the three-body decays, the decay is not isotropic in the Majorana limit; however, the quantity $g_L^2 - g_R^2 \approx 0.02$, suppresses the angular terms in the pure NC case.

6.10 Open charm production

Following the same procedure as the one described in Ref. [?], we estimate the number of strange D mesons to be

$$\mathcal{N}_{D_s} = \frac{\sigma_{c\bar{c}}}{\sigma_{pA}} f_{D_s} = (2.8 \pm 0.2) \times 10^{-6} , \quad (6.47)$$

where $\sigma_{c\bar{c}} = 12 \pm 1 \text{ pb}$ is the proton-target open charm cross section, $\sigma_{pA} = 331.4 \pm 3.4 \text{ mb}$ is the total inelastic proton-target on carbon ($A = {}^{12}\text{C}$) [?] cross section, and $f_{D_s} = 7.7\%$ is the D_s fragmentation fraction [?]. We calculate the open charm production cross section at the leading order in perturbation theory, with a graphite fixed target and a 80 GeV proton p . The correct process to consider is the proton–nucleon interaction, therefore

$$\sigma_{c\bar{c}} \equiv \sigma(pA \rightarrow c\bar{c} + X) \approx A \sigma(pN \rightarrow c\bar{c} + X) ,$$

using the correct Parton Distribution Function (PDF) for a bound nucleon N in the nucleus A . There are four diagrams, shown in figure Fig. 6.10, that contributes to the cross section, but three of them interfere with each other. These cross sections are well-known SM calculations and can be found in Ref. [?].

The integrated cross section is:

$$\begin{aligned} \sigma(pN \rightarrow c\bar{c} + X) = & \int_{\tau_0}^1 dx_1 \int_{\frac{\tau_0}{x_1}}^1 dx_2 \int d\Omega \left[\left(f_{g/p}^1 f_{g/A}^2 + f_{g/p}^2 f_{g/A}^1 \right) \frac{d\sigma_{gg \rightarrow c\bar{c}}}{d\Omega} \right. \\ & \left. + \sum_{q=u,d,s} \left(f_{q/p}^1 f_{\bar{q}/A}^2 + f_{q/p}^2 f_{\bar{q}/A}^1 + f_{\bar{q}/p}^1 f_{q/A}^2 + f_{\bar{q}/p}^2 f_{q/A}^1 \right) \frac{d\sigma_{q\bar{q} \rightarrow c\bar{c}}}{d\Omega} \right], \quad (6.48) \end{aligned}$$

with $\tau_0 = \hat{s}_0/s$ and \hat{s}_0 being the threshold energy at the partonic level and $s = 2m_p(m_p + E_p)$ is the centre of mass energy, given that $m_p \simeq m_n$. The partonic structure of the nucleus is described by the functions $f_{\rho/\eta}^i = f_{\rho/\eta}(x_i, M_F)$, which are interpreted as the probability of finding a parton ρ in the particle η carrying a x_i fraction of the momentum of η , at the energy scale M_F . The two momentum fractions are related by $x_1 x_2 s = \hat{s}$, where the hat symbol denotes the energy of the parton-level process.

We adopt a factorisation scale of $M_F = 2.1 m_c$ for the computation of $\sigma_{c\bar{c}}$, while the renormalisation scale of α_s is set to $\mu_R = 1.6 m_c$, and the charm mass has the value $m_c = (1.28 \pm 0.03)$ GeV. The integration is regulated for $|\cos \theta| < 0.8$, with θ the angle in the centre of mass frame. The theoretical curve in Fig. 7.4(a) of Ref. [?] was used to check our evaluation, and it was successfully reproduced up to NLO corrections. For the calculation we employed LHAPDF [?] and the nCTEQ15 PDF set [?], resulting in $\sigma_{pA \rightarrow c\bar{c}} = (12 \pm 1)$ μb , for an 80 GeV protons on a graphite target.

6.11 Background reduction

We performed a background analysis only for the decay channels with an important discovery potential, and these are $N \rightarrow \nu e^+ e^-$, $\nu e^\pm \mu^\mp$, $\nu \mu^+ \mu^-$, $\nu \pi^0$, $e^\mp \pi^\pm$, and $\mu^\mp \pi^\pm$. The advantage of these channels is that they give the best sensitivities to new physics, thanks to both their high branching ratios and the flux intensity in the region of interest. Moreover, the final state particle are all well-studied particles, most of which leave clean tracks in the detector. As an example of the background reduction using kinematic cuts, we present here the background analysis for a sterile neutrino with mass $m_N = 300$ MeV.

With respect to the following tables, the values presented are in the form “ $\mathcal{X} \rightarrow \mathcal{Y}$ ”, where \mathcal{X} is the per mille (10^{-3}) fraction of background events from mis-identification and \mathcal{Y} is the per mille fraction of irreducible background after the application of data cuts based on kinematic properties. When the value 0×10^{-3} is shown, we mean that less than one background event per million is expected. The average was computed by weighting the flux components contribution to the background, using the respective interaction rate as weights, reported in Tab. 6.4. We assume that the ν_τ and $\bar{\nu}_\tau$ components are not responsible for background events, therefore only the ν_e , ν_μ , and $\bar{\nu}_\mu$ components are studied. The last two rows of the tables are the percentage of signal events retained, after the kinematic cuts are applied to the MC simulation of Majorana and Dirac neutrinos. Because of the overwhelming background, the number of signal events are most of the time substantially influenced.

We group the studied channels in three categories, which have similar kinematic features: two-body decay, which are semi-leptonic, three-body decay channels, which are purely leptonic instead, and decays which can be only detected via photon reconstruction.

6.11.1 Two-body decays

The two-body decays $N \rightarrow e^\pm\pi^\mp$ and $N \rightarrow \mu^\pm\pi^\mp$ are the most promising channels for the detection of a heavy neutrino, being the decay mode with the highest branching ratios. The typical signal is a two charged particle tracks with a common vertex, in a V^0 -like fashion. Muons and pions leave a clean signature in the fine grained tracker and the LArTPC, and electrons are easily reconstructed. They give direct information on the parent particle, being the invariant mass of the process the same as the mass of the decaying neutrino, $m_N^2 = s = m_\ell^2 + m_\pi^2 + 2E_\ell E_\pi - 2|\mathbf{p}_\ell||\mathbf{p}_\pi| \cos\theta$, where θ is the opening angle between the lepton and the pion. Moreover, the two particles are emitted back-to-back in the neutrino reference frame, and, once the system is boosted in the direction of the decaying neutrino, the relative position on the perpendicular plane is preserved. The CC interactions of ν_e and ν_μ are the main background processes, because additional photons or pions can be mis-identified for electrons or muons. We therefore cut on the separation angle between the charged particles, which are very boosted forward, and we request that they are in opposite direction on the plane perpendicular to the beamline. An energy threshold on the reconstructed neutrino, above 5 GeV, is also imposed, as the background events peak at lower energies. The background events are reduced up to a factor $\mathcal{O}(10^4)$, whereas $\sim 46\%$ of the Majorana neutrino events and $\sim 40\%$ of the Dirac neutrino events lie above the cuts.

	$N \rightarrow e^- \pi^+$	$N \rightarrow \mu^- \pi^+$
ν_e	$58.2 \rightarrow 11 \times 10^{-3}$	$0.44 \rightarrow 0 \times 10^{-3}$
ν_μ	$0.11 \rightarrow 0 \times 10^{-3}$	$76.0 \rightarrow 4 \times 10^{-3}$
$\bar{\nu}_\mu$	$0.14 \rightarrow 0 \times 10^{-3}$	$72.9 \rightarrow 10 \times 10^{-3}$
Average	$0.78 \rightarrow 0 \times 10^{-3}$	$74.9 \rightarrow 5 \times 10^{-3}$
Majorana	46.14 %	46.08 %
Dirac	40.48 %	40.00 %

6.11.2 Three-body decays

The three-body decays studied are $N \rightarrow \nu e^- e^+$, $N \rightarrow \nu e^\mp \mu^\pm$, and $N \rightarrow \nu \mu^- \mu^+$. The principle sources of background are mis-reconstructed photons, which promptly converts to electron-positron pairs, or pion tracks that are too long and identified as muons. Despite this, the mis-ID rate is already low as two leptons are needed to identify these channels. However, the background analysis in the case of three-body decays is further complicated by the loss of the light neutrino and so direct information on the parent particle may not be recovered; there is some missing transverse momentum, even though small because of the neutrino lightness. Cuts on the distribution of the transverse momenta of electrons

and muons can therefore help reject background events, which deviate from the beam line direction. We find, nonetheless, that cuts on the invariant mass of the charged lepton system are useful to discriminate signal from background. The energy range considered for the lepton-pairs is different for the channels $\nu e^- e^+$ ($E_{ee} > 2 \text{ GeV}$), $\nu e^\mp \mu^\pm$ ($E_{e\mu} > 4 \text{ GeV}$), and $\nu \mu^- \mu^+$ ($E_{\mu\mu} > 5 \text{ GeV}$), due to different distributions of the background energy spectra in the three cases. The cuts applied to the two-electron channel are the ones with the highest signal selection efficiency, yet reducing the background by a factor ~ 200 . On the contrary, the two-muon channel has the highest mis-identification rate, and so the worst selection success for three-body decays. The electron–muon channel lies in between the other two, presenting though the lowest mis-ID rate. The slightly different behaviours between the kinematics of Majorana and Dirac neutrinos is emphasised by the selection efficiencies of the $\nu e^- e^+$ channel. This tendency is lost as the signal efficiency decreases in the other two channels.

	$N \rightarrow \nu e^+ e^-$	$N \rightarrow \nu e^\pm \mu^\mp$	$N \rightarrow \nu \mu^+ \mu^-$
ν_e	$0.66 \rightarrow 3 \times 10^{-3}$	$4.48 \rightarrow 60 \times 10^{-3}$	$0.11 \rightarrow 0 \times 10^{-3}$
ν_μ	$0.71 \rightarrow 3 \times 10^{-3}$	$0.19 \rightarrow 0 \times 10^{-3}$	$5.42 \rightarrow 7 \times 10^{-3}$
$\bar{\nu}_\mu$	$0.73 \rightarrow 7 \times 10^{-3}$	$0.52 \rightarrow 7 \times 10^{-3}$	$4.72 \rightarrow 9 \times 10^{-3}$
Average	$0.71 \rightarrow 4 \times 10^{-3}$	$0.26 \rightarrow 2 \times 10^{-3}$	$5.31 \rightarrow 9 \times 10^{-3}$
Majorana	68.67 %	44.41 %	36.63 %
Dirac	59.43 %	40.50 %	33.77 %

6.11.3 EM-detected decays

The semi-leptonic decay $N \rightarrow \nu \pi^0$ may only be identified by a correct photon reconstruction, since the neutral pion decays almost 100 % of the time in two photons. This particle is extensively produced in CC and NC neutrino-nucleon interactions, while individual photon background is due to badly reconstructed EM showers, occurring especially in ν_e -CC interactions. If a pair of γ is detected and their invariant mass is compatible with m_{π^0} , the parent pion is reconstructed. Afterwards, we compare the transverse momenta of the single photons with the transverse momentum of their parent particle, and we set constraints on the separation angle between the two γ . We consider only photons with an energy greater than 1 GeV, to avoid the dominant low-energy background. The selection cuts results to be more severe for this mode, leaving signal events just below 20 %, but obtaining a reasonable background reduction of a factor of 500. This detection channel is the most challenging, among those studied, because of the multiple background sources. However, it is one of the decay modes with the highest branching ratio, and with advanced and dedicated techniques [? ?] the reconstruction efficiency can be improved, as well as the background rejection.

$N \rightarrow \nu\pi^0$	
ν_e	$21.0 \rightarrow 58 \times 10^{-3}$
ν_μ	$24.3 \rightarrow 39 \times 10^{-3}$
$\bar{\nu}_\mu$	$26.6 \rightarrow 99 \times 10^{-3}$
Average	$24.4 \rightarrow 43 \times 10^{-3}$
Majorana	18.33 %
Dirac	17.81 %

Appendix A

Appendix 1

This is appendix 1.

 Lorem ipsum dolor sit amet, constetur adipiscing elit, sed do eiusmod tempor incididunt ut labore et dolore magna aliqua. Ut enim ad minim veniam, quis nostrud exercitation ullamco laboris nisi ut aliquip ex ea commodo consequat. Duis aute irure dolor in reprehenderit in voluptate velit esse cillum dolore eu fugiat nulla pariatur. Excepteur sint occaecat cupidatat non proident, sunt in culpa qui officia deserunt mollit anim id est laborum.

Appendix B

Appendix 2

This is appendix 2.

 Lorem ipsum dolor sit amet, constetur adipiscing elit, sed do eiusmod tempor incididunt ut labore et dolore magna aliqua. Ut enim ad minim veniam, quis nostrud exercitation ullamco laboris nisi ut aliquip ex ea commodo consequat. Duis aute irure dolor in reprehenderit in voluptate velit esse cillum dolore eu fugiat nulla pariatur. Excepteur sint occaecat cupidatat non proident, sunt in culpa qui officia deserunt mollit anim id est laborum.

Appendix C

Appendix 3

This is appendix 3.

 Lorem ipsum dolor sit amet, constetur adipiscing elit, sed do eiusmod tempor incididunt ut labore et dolore magna aliqua. Ut enim ad minim veniam, quis nostrud exercitation ullamco laboris nisi ut aliquip ex ea commodo consequat. Duis aute irure dolor in reprehenderit in voluptate velit esse cillum dolore eu fugiat nulla pariatur. Excepteur sint occaecat cupidatat non proident, sunt in culpa qui officia deserunt mollit anim id est laborum.

Bibliography

- [1] A. B. Smith, P. R. Fields, and A. M. Friedman, *Phys. Rev.* **104** (1956) 699.
- [2] A. B. Smith, P. R. Fields, and J. H. Roberts, *Phys. Rev.* **108** (1957) 411.
- [3] A. D. Sakharov, *Pisma Zh. Eksp. Teor. Fiz.* **5** (1967) 32.
- [4] M. Fukugita and T. Yanagida, *Phys. Lett. B* **174** (1986) 45.
- [5] S. Pascoli, S. T. Petcov, and A. Riotto, *Nucl. Phys. B* **774** (2007) 1, [[hep-ph/0611338](#)].
- [6] K. Abe *et al.* [T2K Collaboration], *Phys. Rev. Lett.* **107** (2011) 041801, [[arXiv:1106.2822 \[hep-ex\]](#)].
- [7] Y. Abe *et al.* [Double Chooz Collaboration], *Phys. Rev. Lett.* **108** (2012) 131801, [[arXiv:1112.6353 \[hep-ex\]](#)].
- [8] F. P. An *et al.* [Daya Bay Collaboration], *Phys. Rev. Lett.* **108** (2012) 171803, [[arXiv:1203.1669 \[hep-ex\]](#)].
- [9] J. K. Ahn *et al.* [RENO Collaboration], *Phys. Rev. Lett.* **108** (2012) 191802, [[arXiv:1204.0626 \[hep-ex\]](#)].
- [10] K. Abe *et al.* [Hyper-Kamiokande Collaboration], [[arXiv:1805.04163 \[physics.ins-det\]](#)].
- [11] K. Abe *et al.* [T2K Collaboration], *Phys. Rev. D* **96** (2017) no.9, 092006 (Erratum: *Phys. Rev.D98,no.1,019902(2018)*), [[arXiv:1707.01048 \[hep-ex\]](#)].
- [12] G. Bak *et al.* [RENO Collaboration], *Phys. Rev. Lett.* **121** (2018) no.20, 201801, [[arXiv:1806.00248 \[hep-ex\]](#)].
- [13] D. Adey *et al.* [Daya Bay Collaboration], *Phys. Rev. Lett.* **121** (2018) no.24, 241805, [[arXiv:1809.02261 \[hep-ex\]](#)].
- [14] G. L. Fogli *et al.*, *Phys. Rev. D* **66** (2002) 053010, [[hep-ph/0206162](#)].
- [15] K. Abe *et al.* [Super-Kamiokande Collaboration], *Phys. Rev. D* **97** (2018) no.7, 072001, [[arXiv:1710.09126 \[hep-ex\]](#)].

- [16] K. Abe *et al.* [T2K Collaboration], *Phys. Rev. Lett.* **121** (2018) no.17, 171802, arXiv:1807.07891 [hep-ex].
- [17] A. Atre *et al.*, *JHEP* **0905** (2009) 030, arXiv:0901.3589 [hep-ph].
- [18] M. Drewes and B. Garbrecht, *Nucl. Phys. B* **921** (2017) 250, arXiv:1502.00477 [hep-ph].
- [19] A. V. Artamonov *et al.* [E949 Collaboration], *Phys. Rev. D* **91** (2015) no.5, 052001 (Erratum: *Phys. Rev.D91,no.5,059903(2015)*), arXiv:1411.3963 [hep-ex].
- [20] P. Abreu *et al.* [DELPHI Collaboration], *Z. Phys. C* **74** (1997) 57 (Erratum: *Z. Phys.C75,580(1997)*).
- [21] A. Vaitaitis *et al.* [NuTeV, E815 Collaboration], *Phys. Rev. Lett.* **83** (1999) 4943, [hep-ex/9908011].
- [22] M. Gell-Mann, P. Ramond, and R. Slansky, *Conf. Proc. C* **790927** (1979) 315, arXiv:1306.4669 [hep-th].
- [23] T. Yanagida, *Conf. Proc. C* **7902131** (1979) 95.